June 4, 2025

Relative Timescale of Channel Voltage-Dependence and Channel Density Regulation Impacts Assembly and Recovery of Activity

Yugarshi Mondal[1] Orcid: 0000-0002-7620-8436

Ronald L. Calabrese[2] Orcid: 0000-0001-7135-3469

Eve Marder[1] Orcid: 0000-0001-9632-5448

1: Volen Center and Biology Department, Brandeis University, Waltham, MA 02454

2: Biology Department, Emory University, Atlanta, GA, 30322

Running title: Consequences of Activity-Dependent Channel Voltage-Dependence

Keywords: activation curves, half-activation, activity-dependent regulation, voltage-gated ion channels, homeostasis, intrinsic excitability

ABSTRACT

Neurons can maintain stable activity profiles over their lifetimes despite ion channel turnover over minutes to weeks. Neuronal activity is also influenced by regulating the voltage-dependence of ion channels. How do these two forms of plasticity work together to maintain a stable activity profile? We augment a classical model of activity-dependent ion channel density regulation with a mechanism that adjusts channel voltage-dependence based on activity. These findings reveal that the timescale of these mechanisms shape the specific electrical activity patterns that achieve a target activity profile. Moreover, alterations in channel voltage-dependence can impact a neuron's ability to recover from perturbations. These results highlight a potentially distinct role for activity-dependent regulation of channel voltage-dependence in maintaining stable neuronal activity profiles.

INTRODUCTION

Neurons maintain stable activity patterns over years despite continual turnover in their ion channel composition, which occurs on timescales from days to weeks. Experimental studies have shown that neurons homeostatically regulate both channel number (Desai et al 1999, Haedo & Golowasch 2006, Mizrahi et al 2001, Santin & Schulz 2019, Thoby-Brisson & Simmers 2002, Turrigiano et al 1994, Turrigiano et al 1995, Viteri & Schulz 2023) and channel voltage-dependence (Gasselin et al 2015, Haedo & Golowasch 2006, Thoby-Brisson & Simmers 2002) to stabilize their activity.

These mechanisms have been widely studied through computational modeling, but most of this work has focused on changes in channel number (Abbott & LeMasson 1993, Alonso et al 2023, Golowasch et al 1999, Gorur-Shandilya et al 2020, LeMasson et al 1993, O'Leary et al 2014, Siegel et al 1994, Srikanth & Narayanan 2015). This is largely due to the plethora of work indicating such changes occur (Desai et al 1999, Haedo & Golowasch 2006, Mizrahi et al 2001, Santin & Schulz 2019, Thoby-Brisson & Simmers 2002, Turrigiano et al 1994, Turrigiano et al 1995, Viteri & Schulz 2023). However, this emphasis also reflects the challenges associated with precisely measuring changes in channel voltage-dependence. Inter-neuronal variability in activation and inactivation curves can obscure clear patterns of activity-mediated modifications, especially when analyzed at the population level (Turrigiano et al 1995). As a result, our understanding of how modifications to channel voltage-dependence contributes to activity stability remains limited.

This gap is important to address given the ubiquity of channel voltage-dependence regulation. Neurons modulate voltage-dependence through mechanisms

ranging from rapid post-translational modifications (Fraser & Scott 1999, Johnson et al 1994) or slower processes like subunit synthesis and degradation (Wu et al 2023). These processes are known to be associated with calcium-mediated second messengers. Intracellular calcium is also thought to play an important role in maintaining neuronal activity set points (LeMasson et al 1993, Turrigiano et al 1994). As such, calcium-mediated homeostasis may operate, at least in part, by tuning channel voltage-dependence—yet the consequences of this form of regulation are largely uncharacterized.

To address this, we extended a state-of-the-art computational homeostatic model. This model stabilizes neuronal activity by monitoring intracellular Ca^{2+} concentrations and inserting and deleting ion channels (Alonso et al 2023). To this model, we added a mechanism that alters channel voltage-dependence. Importantly, this model enabled independent control over the timescales of channel number and channel voltage-dependence alterations. This organization of the model let us simulate fast changes in voltage-dependence, such as those driven by phosphorylation, or slower changes, like those resulting from synthesis or degradation of channel subunits. Our central finding is that the timescale of voltage-dependence regulation influences the specific channel configurations a neuron adopts—both while attaining a prespecified activity target and while maintaining it during perturbation.

RESULTS

The Model

To explore how modifications in channel voltage-dependence influence a neuron's capacity to achieve an activity profile as changes in ion channel density occur, we created a computational model. This model was built around a single compartment, Hodgkin-Huxley type conductance-based neuron with seven intrinsic currents (see Turrigiano et al (1995) or Box 1, Supplement 1). The neuron model consisted of a fast Na^+ current, two Ca^{2+} currents, three K^+ currents, a hyperpolarization-activated inward current (I_h), and a leak current. Each current was described by its maximal conductance (number of ion channels) and activation curves. Some currents also possessed inactivation curves as well. The (in)activation curves described the effects of voltage on the opening and closing of the membrane channels.

The activity-dependent regulation of channel number and (in)activation curves employed a strategy that uses intracellular Ca^{2+} concentrations as a proxy for the neuron's activity (Abbott & LeMasson 1993, Alonso et al 2023, Golowasch et al 1999, Gorur-Shandilya et al 2020, LeMasson et al 1993, O'Leary et al 2014, Siegel et al 1994, Srikanth & Narayanan 2015). Specifically, we followed the approach used in Liu et al (1998) and Alonso et al (2023), for altering channel density to guide our approach to altering (in)activation curves. In those models, the intracellular Ca^{2+} concentration and three filters (also called sensors) of the Ca^{2+} concentration were computed. The three sensors were employed to better differentiate between the activity of tonic spiking and bursting neurons (Alonso et al 2023, Liu et al 1998). A target activity profile was chosen by prespecifying the target values of these sensors. These values were selected through

99 trial and error to consistently produce regular bursting across a specific range of initial
100 conditions (see Methods). When deviations from these Ca^{2+} sensor targets were
101 detected, channel densities were altered to up or down regulate the number of channels
102 in the membrane (Alonso et al 2023, Liu et al 1998). Details on how the sensors were
103 computed and how the target activity—defined by the target sensor values—was
104 specified are provided in the Methods.

105 We expanded on these models by incorporating a mechanism that shifts the
106 (in)activation curves in response to deviations from the Ca^{2+} sensor targets. This was
107 accomplished by changing the half-(in)activation voltages of the (in)activation curves,
108 mirroring strategies employed in Liu et al (1998) and Alonso et al (2023). The details of
109 the Model, with their equations and assumptions are described in the Methods section.
110 A brief overview is provided in Box 1.

111 Importantly, the response times of the mechanisms responsible for ion channel
112 insertion and deletion, as well as those for shifts in (in)activation curves, were
113 independently controlled. In the model, these response times were initially set two
114 orders of magnitude apart. This reflected the slower processes of protein synthesis and
115 degradation associated with channel insertion and deletion. This contrasted with faster
116 time scales of post-translational modifications such as channel phosphorylation.
117 Specifically, the timescale for changes in maximal conductance was set at $\tau_g = 600$ s,
118 and the timescale for half-(in)activation shifts at $\tau_{half} = 6$ s. Later, we adjusted the
119 response times of the (in)activation curve shifts. In prior computational studies of
120 activity-dependent regulation, τ_g was set to be less than 10 seconds, substantially faster
121 than the timescales used in our model (Alonso et al 2023, Liu et al 1998). This study

lengthens this timescale and explores the impact of varying the relative timescales of maximal conductance changes (τ_g) and half-(in)activation shifts (τ_{half}).

Bursters Assembled by Activity-Dependent Alterations in Ion Channel Density and Channel Voltage-Dependence

Figure 1 shows the full model, with the two regulation mechanisms in operation. From a set of starting randomly chosen parameters (maximal conductances and half-(in)activations), referred to as Starting Parameters 1 (SP1), the activity-dependent regulation mechanism altered the ion channel density and voltage-dependences to assemble an electrical activity pattern that satisfied the Ca^{2+} targets. The targets were chosen so that a burster self-assembled (see Methods). The final ion channel density and voltage-dependences are shown in the bar graphs (Figure 1A). The first two rows in Figure 1A show the electrical activity of the neuron as the model seeks to satisfy the Ca^{2+} targets. As it does, the model assembled a burster. The second row shows the activity over the entire trace and the first row shows blows up at: the start (a), about 100 minutes (b) and at the end of the simulation (c). At the time shown in (b), the neuron was bursting, but the Ca^{2+} targets had not been achieved. There were two indications that this burster did not satisfy the specified Ca^{2+} targets: (1) the model still continued to adjust the properties of the ion channel repertoire here and (2) α was not yet zero.

Briefly, α measures whether the model has successfully tuned the neuron's ion channel densities and half-(in)activations to create an activity pattern that matches the preset sensor targets; values near zero indicate successful tuning (more in Methods). Even after the model assembles a channel repertoire that satisfies the targets, brief excursions of α away from zero can occur. These excursions exist because the neuron's

electrical activity is quasistable—meaning it may lose/add a spike or experience a slight drop in slow wave amplitude, temporarily causing the sensors to be unsatisfied. When this happens, the model quickly makes minor adjustments to the channel densities and half-(in)activations to restore alignment with the targets (Figure 1—Supplement, Row 2, between minutes 300 and 400). These adjustments are minimal (Figure 1, Rows 3–5).

The third and fourth traces in Figure 1A show how the model altered half-activation and half-inactivation values to meet the Ca^{2+} target. Very early on there were large changes in the activation curves, which then slowly moved to a steady-state value. The fifth trace shows the evolution of maximal conductances. These started to change early on but did so slowly. As the maximal conductances slowly changed, the half-activation curves followed suit, adapting to the new repertoire of ion channels to close the distance to the Ca^{2+} target. Figure 1 Supplement shows the assembly of a burster from a different set of Starting Parameters (maximal conductances and half-(in) activations (SP4)), with qualitatively similar results to those obtained with SP1 but quantitatively different final parameters.

The results shown in Figure 1A require activity-dependent regulation of the maximal conductances. When activity-dependent regulation of the maximal conductances is turned off, the model failed to assemble SP1 into a burster (Figure 1B). This was seen in the other 19 Starting Parameters (SP2-SP20), as well.

In general, when the model was initialized with different Starting Parameters, it produced bursters with different final intrinsic properties. Twenty degenerate bursters (SP1-SP20), conforming to standards specified in Methods, were selected from over 100 bursters produced with different Starting Parameters. Figure 2A shows the activity characteristics of these 20 bursters (Period, Burst Duration, Spike Height, Maximum

170 Hyperpolarization and Slow Wave Amplitude). The left panel of Figure 2B shows the
171 range of conductances in this group. The right panel illustrates the variation in half-
172 (in)activation curves. The asterisks indicate the baseline half-(in)activation values; all
173 neuron models were assembled from starting parameters that lay within ±0.5 mV of
174 these baseline values (see Methods for details).
175
176 *Half-(in)activation Mechanism Timescale Impacts Activity Pattern*
177 In the previous the section, we studied the types of bursters that arose from
178 slowly changing the density of the channel repertoire and quickly altering the half-
179 (in)activations of the resulting repertoire. We next changed the timescale over which we
180 altered half-(in)activations and assessed how the burst characteristics of the population
181 changed (the timescale of channel density alterations remains the same). Figure 3A
182 shows that alterations in the timescale of half-(in)activation alterations significantly
183 impacted the period, interburst interval, spike height, and maximum hyperpolarization
184 of the entire bursting population.
185 The timescale of half-(in)activation alterations also impacted some intrinsic
186 properties of the population. Figure 3B plots the burster assembled with the timescale of
187 half-(in)activation alterations at two extremes: fast and infinitely slow (i.e. off). This
188 visualization is known as a currentscape (Alonso & Marder 2019). In both cases, the
189 resulting burster appeared to terminate using the same mechanism: hyperpolarization
190 via the calcium-activated potassium current. This is seen by the relative contribution the
191 calcium-activated potassium current makes at the point of maximum hyperpolarization
192 (see at the dotted line in Figure 3B). However, the manner in which this current came to
193 dominate the burster termination differs. Note that the burster constructed without

194 half-(in)activation alterations possessed a higher maximal conductance for I_{KCa} than the
195 burster constructed with half-(in)activation alterations (Figure 3C, Mauve dot).
196 Moreover, the latter burster had more depolarized half-activations (Figure 3C, Mauve
197 dot). In fact, this observation held true for SP2-SP20 as well (Figure 3C).
198
199 *Potential Mechanism*
200 To explore why the properties of the resulting bursters depend on the timescale
201 of half-(in)activation adjustments, we examined what happens when SP1 is assembled
202 under different half-(in)activation timescales: (1) fast, (2) intermediate (matching the
203 timescale of ion channel density changes), and (3) infinitely slow (i.e., effectively turned
204 off). The effects of these timescales can be seen by comparing the zoomed-in views of
205 the SP1 activity profiles under each condition (Figure 4).
206 When half-(in)activations are fast, the time evolution of α— which tracks how far
207 the activity pattern is from its targets (see Methods)—shows an abrupt jump as it
208 searches for a voltage-dependence configuration that meets calcium targets (Figure 4A).
209 As this happens, the channel densities are slightly altered, and this process continues
210 again. Slowing the half-(in)activations alterations reduces these abrupt fluctuations
211 (Figure 4B). Making the alterations infinitely slow effectively removes half-(in)activation
212 changes altogether, leaving the system reliant solely on slower alterations in maximal
213 conductances (Figure 4C). Because each timescale of half-(in)activation produces a
214 different channel repertoire at each time step, different timescales of half-(in)activation
215 alteration led the model through a different path in the space of activity profiles and
216 intrinsic properties. Ultimately, this resulted in distinct final activity patterns – all of
217 which were consistent with the Ca^{2+} targets.

218

219 *Half-(in)activation Alterations Contribute to Activity Homeostasis*

220 This model also simulates how the assembled bursters recover their activity
221 following perturbations. In particular, we modeled an increase in extracellular
222 potassium concentration by altering both the potassium reversal potential and the leak
223 reversal potential (see Methods). For these simulations, we used the previously tuned
224 models SP1–SP20. They begin with the homeostatic mechanism engaged but idling
225 because these models already met the prespecified activity targets. However, once
226 extracellular potassium concentration increases, the shifts in reversal potentials cause
227 all 20 models to experience depolarization block. In response, the homeostatic
228 mechanism becomes operative and adjusts the neuron's maximal conductances and
229 half-(in)activations.

230 We anticipated that the perturbation would depolarize the membrane. To
231 accommodate this shift, we increased the allowable deviation for the DC calcium sensor,
232 Δ_D (see Methods), from 0.015 to 0.035. Figure 5A shows SP1's activity before
233 perturbation (blue) and after 265 minutes of recovery (red), under three conditions: fast
234 half-(in)activation regulation, intermediate (same timescale as conductance regulation),
235 and no half-(in)activation regulation. The depolarized membrane potential is evident in
236 the more positive maximum hyperpolarizations during perturbation. Notably, although
237 all three cases eventually re-stabilized to activity patterns that satisfied the calcium
238 targets, the resulting burst patterns were different.

239 SP1 was one of eleven models that successfully recovered under all three
240 homeostatic conditions. Eight models required some form of half-(in)activation
241 modulation to stabilize; in these cases, conductance regulation alone was not sufficient

for recovery. Among these eight, two only recovered when half-(in)activation changes were fast, and another two only recovered when they were slow. Evidently, for some models the ability to recover bursting activity depended on both the presence and speed of half-(in)activation modulation.

Figures 5B and 5C quantify the variability in post-recovery activity patterns and intrinsic parameters across different half-(in)activation regulation timescales. Comparing the fast ($\tau_{half} = 6$ s, blue) and intermediate ($\tau_{half} = 600$ s, green) conditions reveals significant differences in burst period, interburst interval, and spike height (Figure 5B). Notably, these same features also showed significant variation in Figure 3A, where timescale-dependent effects were observed during the initial assembly of bursters. Similarly, the half-activation voltage of the KCa current differs significantly between these two timescales (Figure 5C), paralleling the differences observed in Figure 3C. In models that successfully recovered from perturbation, the timescale of voltage-dependence modulation influenced both the resulting activity patterns and the intrinsic parameters of the stabilized bursters.

DISCUSSION

Timescale of Channel Voltage-Dependence Alterations

While alterations in channel voltage-dependence are known to modulate a neuron's excitability (Levitan 1988), their role in stabilizing a neuron around an activity target has not been extensively explored. This study explores how modifying the *timescale* of voltage-dependence regulation influences both the initial attainment of a target activity pattern and its maintenance during perturbation. While all models met the activity target regardless of whether voltage-dependence modulation was present, recovery after perturbation depended on both the presence and timescale of this mechanism. Furthermore, in both scenarios, the timescale shaped the stabilized neuron's specific activity characteristics and underlying intrinsic parameters. This suggests a general role for the timescale of half-(in)activation modulation in sculpting stable activity states.

Figure 6 provides a conceptual summary of this idea. The space of possible intrinsic parameter configurations (Figure 6A) and electrical activity patterns (Figure 6B) each contain regions that satisfy a given activity target—depicted in blue for activity characteristics and green for intrinsic parameters. The perturbations administered in this study simply shift these target-satisfying regions. When channel gating properties are altered quickly in response to deviations from the target activity, the resulting electrical patterns are shown in Figure 6 as the orange bubble labeled "$\tau_{half} = 6$ s". At a slower timescale of alterations, the activity characteristics and model parameters of the electrical patterns shift, as illustrated by the other orange subregions in Figure 6. This shift conceptually highlights how changing the timescale of alterations to channel

voltage-dependence can move the neuron through different regions within the space of activity characteristics or intrinsic parameters while still maintaining its activity target.

Our simulations show that altering the timescale of the channels' voltage-dependent gating properties impact its activity characteristics. However, what biological processes can implement these alterations? Fast timescale post-translational alterations can be implemented by second messengers that are anchored next to ion channels (Fraser & Scott 1999, Johnson et al 1994) or second messengers that diffuse across the cytosol (Agarwal et al 2016, Zaccolo et al 2006). Phosphorylation by kinases is a commonly studied post-translational modification, however there are other modifications that also occur on these time scales, such as S-nitrosylation (Broillet 1999). On slower timescales, the neuron can modulate the transcription and translation of these auxiliary subunits based on intracellular calcium levels. For instance, Potassium Channel-Interacting Proteins are known to be controlled by CREB (Wu et al 2023).

Biological Relevance

One application for the simulations involving the self-assembly of activity may be to model the initial phases of neural development, when a neuron transitions from having little or no electrical activity to possessing it (Baccaglini & Spitzer 1977). As shown in Figure 6, the timescale of (in)activation curve alterations define a neuron's activity characteristics and intrinsic properties. As such, neurons may actively adjust these timescales to achieve a specific electrical activity aligned with a developmental phase's activity targets. Indeed, developmental phases are marked by changes in ion channel density and voltage-dependence, leading to distinct electrical activity at each stage (Baccaglini & Spitzer 1977, Gao & Ziskind-Conhaim 1998, Goldberg et al 2011,

303 Hunsberger & Mynlieff 2020, McCormick & Prince 1987, Moody & Bosma 2005,
304 O'Leary et al 2014, Picken Bahrey & Moody 2003).

305 Additionally, our results show that activity-dependent regulation of channel
306 voltage-dependence can play a critical role in restoring neuronal activity during
307 perturbations (Figure 5). Specifically, the presence and timing of half-(in)activation
308 modulation influenced whether the model neuron could successfully return to its target
309 activity pattern. Many model neurons only achieved recovery when a half-(in)activation
310 mechanism was present. Moreover, the speed of this modulation shaped recovery
311 outcomes in nuanced ways: some model neurons reached their targets only when
312 voltage-dependence was adjusted rapidly, while others did so only when these changes
313 occurred slowly. These observations all suggest that impairments in a neuron's ability to
314 modulate the voltage-dependence of its channels may lead to disruptions in activity-
315 dependent homeostasis. This may have implications for conditions such as addiction
316 (Kourrich et al 2015) and Alzheimer's disease (Styr & Slutsky 2018), where disruptions
317 in homeostatic processes are thought to contribute to pathogenesis.

318 In conclusion, our findings suggest that when a neuron begins from a state of no
319 activity and small randomly specified channel densities, changes in channel density are
320 essential for attaining activity. In this context, activity-dependent changes in channel
321 voltage-dependence alone are insufficient to attain bursting (cf Figure 1B). Based on this
322 evidence alone, one might conclude that shifts in (in)activation curves have negligible
323 impact, effectively being overshadowed by the larger changes in excitability driven by
324 alterations in channel density. This perspective aligns with a common assumption in
325 systems analysis: that short- and long-timescale processes are sufficiently distinct and

326 can be studied independently without significant interaction. However, our results
327 demonstrate that fast shifts in half-(in)activation constrain the types of activity
328 characteristics and intrinsic properties a neuron ultimately expresses (Figure 6). These
329 fast alterations, while subtle, manifest over long timescales required to assemble
330 activity. This study exemplifies how interactions between processes operating on
331 different timescales can influence one another. Such principles are particularly relevant
332 for understanding multiscale interactions in neuroscience, such as the connections
333 between subcellular, cellular, and network-level properties (Bhalla 2014, Marom 2010).

334 METHODS

335 *Details of the Model and its Implementation*

336 Box 1 presents a scheme for the equations used in the model: a Hodgkin-Huxley
337 type equation with 7 intrinsic currents, Ca^{2+} sensors, and an activity-dependent
338 regulation mechanism.

339 The Hodgkin-Huxley type neuron consisted of 7 intrinsic currents (Box 1,
340 Supplement 1, Equations 1-3) and an intracellular Ca^{2+} concentration calculation (Box 1,
341 Supplement 1, Equation 4). The neuron's capacitance (C) was set to 1 nF. The currents
342 were labeled by the index i and were in order: fast sodium (I_{Na}), transient calcium (I_{CaT}),
343 slow calcium (I_{CaS}), hyperpolarization-activated inward cation current (I_H), potassium
344 rectifier (I_{Kd}), calcium-dependent potassium (I_{KCa}), and fast transient potassium (I_A).
345 Additionally, there was a leak current (I_L). The maximal conductances were given by $\bar{g}_i$.
346 Activation and inactivation dynamics were given by m_i and h_i, respectively. The
347 exponents q_i were given by 3,3,3,1,4,4,3, respectively. The equilibrium/reversal
348 potentials of the sodium current, hyperpolarization activated cation current, potassium
349 currents, and leak current were +30 mV, -20 mV, -80 mV and -50 mV respectively. The
350 calcium equilibrium potential was computed via the Nernst Equation (Box 1,
351 Supplement 1, Equation 5) using the computed internal Ca^{2+} concentration ($[Ca^{2+}]_i$) and
352 an external Ca^{2+} concentration of 3 mM (temperature was 10 ^{o}C).

353 We modeled perturbations in neuronal activity by a 2.5-fold increase in
354 extracellular potassium concentration. Using the Nernst equation, this shift corresponds
355 to a change in the potassium reversal potential from −80 mV to −55 mV. We assume
356 that leak current in our model includes a potassium component, so that the perturbation

also impacts the leak reversal potential. Additionally, assuming that the remaining leak current comes from sodium channels, we can compute how to perturb the leak reversal potential. The leak maximal conductance for our model is fixed at .01 μS. The new leak reversal potential was calculated using standard computation involving the conductance-weighted average of potassium and sodium reversal potentials, yielding a valued of approximately -32 mV.

The activation curves and inactivation curves were given by $m_{i,\infty}$ and $h_{i,\infty}$. Their associated time constants were τ_{m_i} and τ_{h_i}, respectively. The (in)activation curves and their associated time constants were functions of the membrane voltage, V (see tables in Box 1, Supplement 1). Note that I_{KCa} had an activation curve that depends on internal Ca^{2+} concentration. The internal calcium concentration was computed using I_{CaT} and I_{CaS} (Box 1, Supplement 1, Equation 4).

There were three Ca^{2+} sensors that responded to different measures associated with fluctuations of $[Ca^{2+}]_i$ during a burst. They were used to determine how close these measures are to their targets. These measures were the amount of $[Ca^{2+}]_i$ that entered the neuron: as a result of the slow wave of a burst (S), as a result of the spiking activity of a burst (F), and on average during a burst (D). They were computed using Equations 6-8 (Box 1, Supplement 2). Each sensor had a corresponding target value – $\bar{S}, \bar{F}, \bar{D}$ – which represented the target activity pattern.

The model computed moving averages of the mismatch between each sensor and its target, denoted, E_S, E_F, and E_D (Equations 9–11, Box 1, Supplement 2). These averages were taken over a two-second window ($\tau_S = 2000$ ms). allowing the model to smooth out short-term fluctuations and capture sustained deviations from the target.

Ideally, E_S, E_F, and E_D, are zero, however, ongoing membrane fluctuations, such as bursting or spiking still created small variations in these measures. Allowable tolerances are specified in the model as, Δ_s, Δ_F, and Δ_D, respectively. The moving averages of the mismatches between the calcium sensors and their targets are compared against the allowable tolerances and combined in Equation 12 (Box 1, Supplement 2) to create a "match score", S_F (Equation 12).

To compute this match score, we adapted a formulation from Alonso et al (2023), who originally used a root-mean-square (RMS) or L^2 norm to combine the sensor mismatches. In that approach, each error (E_S, E_F, and E_D) is divided by its allowable tolerance (Δ_s, Δ_F, and Δ_D) to produce a normalized error. These normalized errors are then squared, summed, and square-rooted to produce a single scalar score that reflects how well the model matches the target activity pattern.

In our version, we instead used an L^8 norm, which raises each normalized error to the 8th power before summing and taking the 1/8th root. This formulation emphasizes large deviations in any one sensor, making it easier to pinpoint which feature of the activity is limiting convergence. By amplifying outlier mismatches, this approach provided a clearer view of which sensor was driving model mismatch, helping us both interpret failure modes and tune the model's sensitivity by adjusting the tolerances for individual sensor errors.

Although the L^8 norm emphasizes large deviations more strongly than the L^2 norm, the choice of norm does not fundamentally alter which models can converge—a model that performs well under one norm can also be made to perform well under another by adjusting the allowable tolerances. The biophysical mechanisms by which

neurons detect deviations from target activity and convert them into changes in ion channel properties are still not well understood. Given this uncertainty, and the fact that using different norms ultimately shouldn't affect the convergence of a given model, the use of different norms to combine sensor errors is consistent with the broader basic premise of the model: that intrinsic homeostatic regulation is calcium mediated.

Equations 13 and 14 were used to evaluate whether the match score was sufficient for the model to cease altering maximal conductances and (in)activation curves, indicating that the target had been achieved. In Equation 14 (Box 1, Supplement 2), the "match score" was compared to a preset threshold value the model would accept, ρ. This equation returned 1 if the match score is below ρ, a 0 if the match score is above ρ, and some number in between 0 and 1 if the match score was close to the threshold, ρ. Equation 13 (Box 1, Supplement 2) then effectively computed a 2 second time average of Equation 14. Equation 13 was an activity sensor, α, that was plotted in Figure 1. It took the value zero when all three Ca^{2+} sensors were close to the Ca^{2+} targets but remained close to one otherwise. The value of this activity sensor was used to slow the evolution of maximal conductances and half-(in)activations as the Ca^{2+} sensors reached their targets. It also served as a measure for how well the model satisfied the Ca^{2+} sensors. In this model, $\rho = 0.3$. The "sharpness" of the threshold at $\rho = 0.3$ was set by Δ_α. We set $\Delta_\alpha = 0.01$ indicating that when the match score, S_f, was greater than ~0.32, the model considered the calcium targets satisfied.

Using the information regarding how well the Ca^{2+} sensors were satisfied, the model regulated conductance densities and (in)activation curves. The maximal conductances $\bar{g}_i$, and the ion channel voltage-sensitives, as measured by activation

curve shifts, $V_{s_i^m}$, and inactivation curve shifts, $V_{s_i^h}$, from their specified locations ($V_{\hat{m}_{i,1/2}^0}$ for activation curves and $V_{\hat{h}_{i,1/2}^0}$ for inactivation curves), were altered by the model in response to deviations from the calcium targets (Box 1, Supplement 3, Equations 15-17). The latter were adjusted on a time scale given by τ_{half} and the former by τ_g. The index i ran from 1 through 7 for the maximal conductances (Equation 15) and half-(in)activations (Equation 16). In Equation 17, the index only took on a subset of values: $i = 1,2,3,7$ – because only some intrinsic currents in this model had inactivation (the associated currents being listed above).

Equations 16 and 17 were new equations added to the model. They were built similarly to Equation 15. In Equation 15, the maximal conductances were altered when the calcium sensors didn't match their targets. There are two parts to Equation 15: a part that converts calcium sensor mismatches into changes in maximal conductances and a cubic term. The cubic term prevents unbounded growth in the maximal conductances. We set the constant associated to the cubic term, γ, to 10^{-7}. The other term adjusted the maximal conductance based on fluctuations of calcium sensors from their target levels. The parameters A_i, B_i and C_i reveal how the sensor fluctuations contribute to the changes of each maximal conductance. These values were provided in Liu et al (1998). Importantly, note that this term is multiplied by $\bar{g}_i$, which prevents the maximal conductance from becoming negative and scales the speed of evolution so that smaller values evolve more slowly and larger values evolve more quickly. As such, multiplication by $\bar{g}_i$ effectively induced exponential changes in the maximal conductance, allowing $\bar{g}_i$ to vary over orders of magnitude.

Equations 16 and 17, introduced in this paper, enable the adjustment of the ion-channel voltage dependence. Equations 16 and 17 also each have two components: a component that converts calcium sensor mismatches into changes in half-(in)activations and a cubic term. The cubic term prevents unbounded translations. The cubic term's constant, $\hat{\gamma}$, was set to 10^{-5}. The other term adjusts the half-activations (Equation 16) and half-inactivation (Equation 17) based on deviation of calcium sensors from their target levels.

Finally, we discuss how the coefficients A_i, B_i and C_i in Equation 15, and the corresponding parameters in Equation 16 and 17 were chosen. The same coefficients used to adjust maximal conductances were used for the inactivation curve shifts, $\hat{\hat{A}}_i$, $\hat{\hat{B}}_i$, and $\hat{\hat{C}}_i$. The coefficients of the activation curve shift are their negatives, $\hat{A}_i$, $\hat{B}_i$, and $\hat{C}_i$. To understand this choice, consider a scenario where the neuron is bursting more rapidly than desired. In that case, then $F > \bar{F}$, $S > \bar{S}$, and $D > \bar{D}$. To reduce the excitability of the neuron, we made the depolarizing current, for example, I_{Na}, harder to activate, by shifting the activation curve of I_{Na} to a more depolarizing potential. This implies $\frac{dV_{s_1^m}}{dt} > 0$. Therefore, the coefficients $\hat{A}_i$, $\hat{B}_i$, and $\hat{C}_i$ must be non-positive. The coefficients for I_{Na} in Liu et al (1998) were given as $A_1 = 1$, $B_1 = 0$ and $C_1 = 0$ and were chosen so that $\frac{d\bar{g}_1}{dt} < 0$, thereby decreasing the maximal conductance of sodium in the same scenario. So, we flipped the signs to give $\widehat{A_1} = -1$, $\widehat{B_1} = 0$ and $\widehat{C_1} = 0$. In this way, only the F Ca^{2+} sensor contributed to the modulation of I_{Na}, but the activation curves were now adjusted to promote homeostasis. Furthermore, the model makes it harder to de-inactivate I_{Na} by shifting its inactivation curve to more hyperpolarized values $\left(\frac{dV_{s_1^h}}{dt} < 0\right)$. In the scenario

in which the activity sensors are greater than their activity targets, this corresponds to setting $\hat{\hat{A}}_1 = 1$, $\hat{\hat{B}}_1 = 0$, and $\hat{\hat{C}}_1 = 0$.

A similar logic can be used to understand how the activation curves of the outward currents were adjusted. In the scenario described above, the neuron was made less excitable by increasing the amount of an outward current, for example I_A. This was done by increasing its maximal conductance or moving its activation curve to more hyperpolarized values. Liu et al (1998) assigned the coefficients $A_7 = 0,\ B_7 = -1$ and $C_7 = -1$ to adjust the maximal conductance of I_A. In this scenario where all sensors are above their targets, this implies $\frac{d\bar{g}_7}{dt} > 0$. Following the prescription we outlined above, flipping the signs gives $\widehat{A_7} = 0,\ \widehat{B_7} = 1$ and $\widehat{C_7} = 1$. This, in turn, implied $\frac{dV_{s_7^m}}{dt} < 0$ – creating hyperpolarizing shifts in I_A's activation curve when the activity is greater than its target, as we expect. In a similar spirit, we assign the coefficients $\hat{\hat{A}}_7 = 0$, $\hat{\hat{B}}_7 = -1$, and $\hat{\hat{C}}_7 = -1$, so that I_A's inactivation curve shifts to more depolarizing potentials $\left(\frac{dV_{s_7^h}}{dt} > 0\right)$ to make it easier to de-inactivate.

Note, the coefficients in Liu et al (1998) don't perfectly correspond with this reasoning. In Liu et al (1998), some coefficients were assigned values to ensure convergence of the model. Still, we followed the prescription outlined above (Box 1, Supplement 3, Table 1).

Starting Parameters

The model has 40 ordinary differential equations: 13 equations describe the neuron's electrical activity, 9 equations describe calcium sensor components, and 18

491 equations alter the maximal conductances and half-(in)activations (Box 1). This means
492 we needed to specify 40 starting values for the model. We defined starting parameters
493 (SPs), as the bursters the model assembles from a particular set of randomly chosen
494 starting maximal conductances and half-(in)activations. The maximal conductances
495 were randomly selected between 0.3 nS and 0.9 nS and half-(in)activation shifts are
496 randomly offset between -0.5 mV and +0.5 mV from their specified half-(in)activation
497 values ($V_{\hat{m}^0_{i,1/2}}$ and $V_{\hat{h}^0_{i,1/2}}$ in Box 1, Supplement 1, Table 2). Other starting values were
498 $V = -50$ mV and the gating variables of activation and inactivation were randomly
499 selected between 0.2 and 0.3. The starting value of intracellular calcium concentration
500 was set as $[Ca^{2+}]_i = 0.4\ \mu$M. Equations 9-11 (Sensor Errors) and Equation 13 (Activity
501 sensor, α) were initialized with the value 1. H_X (Equation 7) and M_X (Equation 6) were
502 initialized to 0 and 1, respectively.

503 The random initialization of gating variables was not expected to significantly
504 impact the formation of an activity profile that satisfied the activity target. Bursters may
505 exhibit bistability if they are initialized with different gating variables. However, this is
506 for a fixed set of maximal conductances and half-(in)activations. Any bistability in the
507 initially specified profile was likely lost as the model altered the maximal conductances
508 and half-(in)activations.

509 The model was integrated using the Tsitouras 5 implementation of Runga-Kutta
510 4(5) in Julia's DifferentialEquations.jl package (Tsitouras 2011). The simulation was
511 saved every 0.5 milliseconds regardless of step size (step size of the integrator was
512 adaptive and left unspecified). Maximum number of iterations was set to 10^{10} and
513 relative tolerance was set to 0.0001.

514 *Burster Measurements*

515 We defined regular bursters as activity patterns that exhibited groups of spikes
516 separated by regular quiescent gaps in activity. To identify bursters, we measured the
517 following activity characteristics: period, burst duration, interburst interval, spike
518 height, maximal hyperpolarization, and slow wave amplitude. Peaks were identified as
519 local maxima in the activity pattern. We used the `findpeaks` function in MATLAB on
520 the last 90 secs of activity to identify local maxima in the trace, setting the minimum
521 'prominence' at 2. The latter parameter rejected certain local maxima from counting as
522 peaks. This parameter is one we arrived at by trial and error. Figures 7-B1 and 7-B2
523 show red arrows where this function identified peaks. Note in Figure 7-B2, panels A-C
524 have local maxima that are not counted as peaks (there is one local maxima following
525 the sequence of peaks in the burst). The choice of 'prominence' in the 'findpeaks'
526 function was intentionally set to exclude these. To find troughs, we took the negative of
527 the activity profile and found local maxima using the `findpeaks` function. For this, the
528 same 'prominence' parameter was used over the same time window. The arrows in
529 Figure 7C show an example of what was identified by the algorithm as a peak in this
530 case. Troughs were defined as the negative of the identified points. The red arrow in
531 Figure 7C shows the maximum hyperpolarization of a cycle obtained using the method
532 described below. The green arrows are the troughs associated with each spike in the
533 burst (Figure 7C).

534 Maximum hyperpolarization was found as follows. First all troughs were
535 identified in the manner described above. Then, starting at -85 mV, we checked whether
536 there were any troughs below this value. If there were none, we incremented by 1 mV to
537 -84 mV and checked again if there were any troughs below this value. This process was

538 repeated until troughs were detected. The troughs identified this way demarcated the
539 ends of a cycle in the activity pattern. They were averaged to obtain the maximum
540 hyperpolarization measurement for the activity pattern.

541 The time interval between successive maximum hyperpolarizations in the activity
542 was used to measure the cycle period (Figure 7D). We averaged these cycle period
543 measurements to give a measurement for the activity pattern's period. To obtain the
544 burst duration, we segmented the activity pattern into cycles using the time of
545 maximum hyperpolarization. The burst duration of a cycle was measured as the time
546 between the first and last spike in the cycle (Figure 7C). The interburst interval of the
547 cycle was computed by subtracting the cycle's burst duration from the cycle period.

548 To measure the slow wave amplitude, we identified the troughs of each cycle. The
549 slow wave amplitude of a cycle is the difference between the maximum
550 hyperpolarization (Figure 7D, red arrow) during a cycle and the average of the
551 membrane potential at the troughs associated with each spike in a burst (Figure 7D,
552 green arrows). The slow wave amplitudes across all cycles were averaged to obtain a
553 measurement for the activity pattern's slow wave amplitude.

554 The spike height was obtained by finding the peaks of the membrane potential
555 during each cycle. A measure for the cycle's spike height was obtained by averaging over
556 all peaks, subtracting the cycle's maximum hyperpolarization, then subtracting the
557 cycle's slow wave amplitude. This value was averaged over all cycles to obtain a measure
558 of the activity pattern's spike height.

559 We distinguished regular bursting from tonic spiking or irregular bursting using
560 the following procedure. We classified an activity pattern as a regular burster when: 1)
561 there was more than 1 spike per cycle, 2) the maximum hyperpolarization

measurements for all cycles were within 3 mV of one another, and 3) the spikes per cycle varied by no more than 1 spike. The first condition eliminated tonic spiking, the second condition is a crude measure to check that the average voltage wasn't increasing, and the third checked for irregular bursting. In addition, we verified that the cycle-to-cycle measurements exhibited low variability to ensure the appropriateness of averaging across all cycles. The relative standard deviation for all cycle-to-cycle measurements was less than 3% for the assembled bursters.

Activity Target Selection

We needed a set of sensor targets that *consistently* produced regular bursters, regardless of the starting parameters selected. To determine whether a set of calcium targets consistently produced a burster, we monitored the activity sensor α. α approached 0 when the calcium sensors were close to their specified targets. There were small oscillations in α that resulted from calcium fluctuations associated with the neuron's activity. These fluctuations were smoothed out by taking a running average over the 8 previous seconds. When a simulation fell below $\alpha = 0.02$ for the last time and remained there for 100 minutes, we considered the simulation to have "*assembled*" a burster that satisfied the calcium targets. For simulations involving elevated extracellular potassium concentration, this criterion was adjusted: a model was considered to have satisfied the calcium targets if the moving average of α fell below 0.02 and remained there for at least 5 minutes. This change was made because the perturbation simulations were shorter.

To ensure the activity pattern obtained did not depend on feedback from the activity regulation mechanism, the mechanism was turned off ($\tau_{half} = \infty$, $\tau_g = \infty$) and

the simulation run for an additional 9000 secs to ensure $\alpha < .02$ for the duration. This step was taken in the initial generation of bursters (111 in total, described below), but not for the analysis where the time constants of the half-activation alterations were changed from $\tau_{half} = 6$ s.

'*Consistently*', in this context, meant that the model assembled bursters from over 95% of the randomly chosen starting parameters. The remaining simulations did not complete assembly within the given simulation period. For the calcium targets we found ($\bar{S} = 0.03, \bar{F} = 0.25$, and $\bar{D} = 0.02$), the model 'consistently' produced bursters. To obtain these targets, we tried different combinations of calcium targets until a suitable set of targets consistently produced regular bursters.

Groups of Bursters

Using the obtained calcium targets, we assembled a total of 111 regular bursters from a wide range of randomly initialized starting parameters. To create a representative subset of this population, we selected a Group of 20 bursters through successive rounds of restriction. The goal was to form a set of models that shared similar burst periods but varied in other activity characteristics and intrinsic properties. This allowed us to assess how different bursters responded to changes in the speed of half-(in)activation alterations as the model attempted to reach or maintain its activity target.

We first filtered the 111 models by slow wave amplitude, retaining only those with amplitudes less than 25 mV. This excluded models with unusually large oscillations and preserved activity patterns with waveforms similar to those shown in Figure 7C, reducing the pool to 80 models. The distribution of these bursters' periods are shown in

607 Figure 7A. The peak of this distribution is between 380 and 500 ms. We further
608 narrowed the population by selecting bursters around the peak of this distribution
609 (Figure 7A, highlighted in Red), resulting in 33 bursters (the "selection group"). This
610 range contained about 30% of the distribution.

611 In the next round of restriction, we obtained a Group of 20. We ordered the
612 bursters from shortest to longest period. For each burster from the 3rd to the 31st
613 position, we examined the two bursters immediately preceding and the two bursters
614 immediately succeeding in this sorted list and computed the range of burst periods
615 across these five bursters (Figure 7B). This method provided a rough estimate of the
616 variability in periods among neighboring bursters. The burster exhibiting the smallest
617 inter-instance period variability was selected as the first member of the Group of 20
618 (Figure 7B, Red Arrow). This first burster is referred to as SP1 in Figure 1 (also shown in
619 Figure 7C) and has a period of about 416 ms. In the second step, we symmetrically
620 expanded the inter-instance period range around SP1's period by 20%. We randomly
621 selected an additional 20 models from this group to create the Group of 20.

622 *Model Assumptions*

623 This model of channel voltage-dependence alterations is based on certain
624 assumptions. The concept outlined in Figure 6 is not expected to depend on these
625 choices. However, examining these assumptions reveals additional insights.

626 The model makes two simplifications on how quickly channel gating properties
627 can be altered. First, the model assumes a single, uniform time constant for modifying
628 all intrinsic currents. In reality, each intrinsic current is likely influenced by a
629 combination of mechanisms. For example, the relative contributions of anchored second

630 messengers and freely diffusing kinases in phosphorylating key residues in L-Type
631 calcium channels are not well understood and may well involve both processes (Weiss et
632 al 2013). Consequently, the timescale of modulation for I_{CaS}—the current to which L-
633 Type calcium channels putatively contributes—likely represents a weighted average of
634 these mechanisms. Similarly, I_{Kr}, is modulated by PIP2 (a metabolite of calcium-
635 mediated second messenger pathways) and a beta subunit (Li et al 2011). While the
636 presence or absence of PIP2 can change on a fast timescale, the synthesis of the beta
637 subunit occurs over much slower timescales, resulting in mixed temporal dynamics.
638 These examples illustrate that the balance between fast and slow regulatory mechanisms
639 likely varies among intrinsic currents, complicating the assumption of a single time
640 constant. Second, our framework assumes post-translational modifications are removed
641 as quickly (or slowly) as they are added. This simplification fails to account for processes
642 where rapid calcium increases lead to prolonged downstream effects. For instance, the
643 calcium-mediated second messenger CaMKII undergoes autophosphorylation, enabling
644 a brief calcium signal to induce long-lasting changes in protein activity (Hudmon &
645 Schulman 2002, Kennedy 1989). This autophosphorylation is known to influence
646 intrinsic excitability of neurons (Sametsky et al 2009) and may modulate the voltage-
647 dependence of Ca_V2 channels (Jiang et al 2008), which putatively contribute to I_{CaS}.
648 Accounting for these processes would require a more complex model capable of
649 capturing asymmetries in modification rates.

650 Another assumption we make is that there are limits on the extent to which
651 (in)activation curves can shift. This limitation is implemented through the cubic term in
652 Equations 16 and 17. These constraints reflect the fact that shifts in activation curves are
653 not unlimited. For example, while cAMP can shift the half-activation of I_h, this effect

654 saturates at high cAMP concentrations (Difrancesco & Tortora 1991). In this study,
655 however, a uniform constraint is applied across all intrinsic currents. In reality, different
656 intrinsic currents likely have unique limits on how much they can shift, requiring
657 distinct functional forms to model their unique restrictions.

658 Furthermore, we assumed that activity-dependent alterations in channel voltage-
659 dependence are implemented by changing half-(in)activations. We have not, however,
660 considered the (in)activation curve's slope or the gating variable's time constant. In this
661 study, the gating variable's voltage-dependent time constant shift by the same amount
662 as the half-(in)activation. This preserves how quickly the gating variable respond to
663 changes in voltage – regardless of where the activation curve is centered. However, this
664 coupling between the time constant and the activation curve is not necessarily required.
665 For instance, activity-dependent shifts in voltage-dependent time constants have been
666 observed without concomitant shifts in activation curves (Thoby-Brisson & Simmers
667 2002). The voltage dependence of the time constant can, in principle, change in other
668 ways as well. Also, we presume that the slopes of the (in)activation curves do not
669 respond to changes in activity. The slope of (in)activation curves defines the steepness of
670 the voltage dependence for ion channel gating, thereby influencing the voltage
671 sensitivity of the transition between states (e.g., from closed to open or from inactivated
672 to deinactivated). In this model, the slopes of these curves are held constant.
673 Consequently, the voltage ranges remain fixed regardless of shifts in the centering of the
674 activation or inactivation curves. Nonetheless, with certain calcium-activated potassium
675 currents, the center and slope of the activation curve depends on calcium concentration
676 (Wang & Brenner 2006). To the extent that calcium entry during activity initiates

677 downstream signaling processes that alter ion channel function, this observation
678 supports the idea that activity could influence the slope of the I_{KCa} activation curve.
679 In the model, the same activity targets are used to drive changes in both channel
680 density and voltage dependence. This assumes extensive crosstalk between the calcium
681 pathways posited to be responsible for ion channel insertion, deletion, and post-
682 translational modifications. Nonetheless, the extent to which this crosstalk occurs is not
683 known, although, it is known that cells can detect the temporal patterns and specific
684 pathways of calcium entry, leading to specific activity-dependent changes (Bito et al
685 1997, Fields et al 1997, Gallin & Greenberg 1995). Therefore, it is likely that activity-
686 induced calcium influxes trigger changes along distinct pathways – with some impacting
687 only channel gating properties, some impacting channel density, and some impacting
688 both.
689 It is not necessarily true that all activity-dependent changes in the properties of
690 intrinsic currents are directly controlled by calcium influx. For example, neurons
691 coregulate I_A and I_H expression, so that a change in one current is associated with a
692 change in the other (MacLean et al 2005). Neuromodulatory environment may also play
693 a role in coordinating ion channel levels (Khorkova & Golowasch 2007). In such cases,
694 one may use this model for the channels that are controlled by activity and augment it
695 by explicitly modelling the remaining mechanisms that are independent of activity.
696

DATA AVAILABILITY

The code and parameters required to reproduce the results in this work are accessible and at Zenodo. Repository: [https://github.com/YugarshiM/fastTimescaleHomeostasis] [DOI: 10.5281/zenodo.12585617]

ACKNOWLEDGMENTS

The authors acknowledge the support of NIMH (R01MH046742), NINDS (R35NS097343), and The Swartz Center for Theoretical Neuroscience at Brandeis University. YM acknowledges valuable discussions with lab members. Also, YM acknowledges assistance with code preparation from Gwendolyn Harris.

709 REFERENCES

710 Abbott L, LeMasson G. 1993. Analysis of neuron models with dynamically regulated conductances.
711 *Neural Computation* 5: 823-42
712 Agarwal SR, Clancy CE, Harvey RD. 2016. Mechanisms Restricting Diffusion of Intracellular cAMP.
713 *Scientific Reports* 6: 19577
714 Alonso LM, Marder E. 2019. Visualization of currents in neural models with similar behavior and
715 different conductance densities. *Elife* 8: e42722
716 Alonso LM, Rue MCP, Marder E. 2023. Gating of homeostatic regulation of intrinsic excitability produces
717 cryptic long-term storage of prior perturbations. *Proc Natl Acad Sci U S A* 120: e2222016120
718 Baccaglini PI, Spitzer NC. 1977. Developmental changes in the inward current of the action potential of
719 Rohon-Beard neurones. *J Physiol* 271: 93-117
720 Bhalla US. 2014. Molecular computation in neurons: a modeling perspective. *Curr Opin Neurobiol* 25: 31-
721 7
722 Bito H, Deisseroth K, Tsien RW. 1997. Ca^{2+}-dependent regulation in neuronal gene expression. *Curr Opin*
723 *Neurobiol* 7: 419-29
724 Broillet MC. 1999. S-nitrosylation of proteins. *Cell Mol Life Sci* 55: 1036-42
725 Desai NS, Rutherford LC, Turrigiano GG. 1999. Plasticity in the intrinsic excitability of cortical pyramidal
726 neurons. *Nature Neuroscience* 2: 515-20
727 Difrancesco D, Tortora P. 1991. Direct activation of cardiac pacemaker channels by intracellular cyclic
728 AMP. *Nature* 351: 145-47
729 Fields RD, Eshete F, Stevens B, Itoh K. 1997. Action potential-dependent regulation of gene expression:
730 temporal specificity in Ca^{2+}, cAMP-responsive element binding proteins, and mitogen-activated
731 protein kinase signaling. *J Neurosci* 17: 7252-66
732 Fraser IDC, Scott JD. 1999. Modulation of Ion Channels. *Neuron* 23: 423-26
733 Gallin WJ, Greenberg ME. 1995. Calcium regulation of gene expression in neurons: the mode of entry
734 matters. *Curr Opin Neurobiol* 5: 367-74
735 Gao BX, Ziskind-Conhaim L. 1998. Development of ionic currents underlying changes in action potential
736 waveforms in rat spinal motoneurons. *J Neurophysiol* 80: 3047-61
737 Gasselin C, Inglebert Y, Debanne D. 2015. Homeostatic regulation of h-conductance controls intrinsic
738 excitability and stabilizes the threshold for synaptic modification in CA1 neurons. *J Physiol* 593:
739 4855-69
740 Goldberg EM, Jeong HY, Kruglikov I, Tremblay R, Lazarenko RM, Rudy B. 2011. Rapid developmental
741 maturation of neocortical FS cell intrinsic excitability. *Cereb Cortex* 21: 666-82
742 Golowasch J, Casey M, Abbott LF, Marder E. 1999. Network stability from activity-dependent regulation
743 of neuronal conductances. *Neural Comput* 11: 1079-96
744 Gorur-Shandilya S, Marder E, O'Leary T. 2020. Activity-dependent compensation of cell size is vulnerable
745 to targeted deletion of ion channels. *Scientific reports* 10: 15989
746 Haedo RJ, Golowasch J. 2006. Ionic mechanism underlying recovery of rhythmic activity in adult isolated
747 neurons. *J Neurophysiol* 96: 1860-76
748 Hudmon A, Schulman H. 2002. Neuronal Ca^{2+}/calmodulin-dependent protein kinase II: the role of
749 structure and autoregulation in cellular function. *Annu Rev Biochem* 71: 473-510
750 Hunsberger MS, Mynlieff M. 2020. BK potassium currents contribute differently to action potential
751 waveform and firing rate as rat hippocampal neurons mature in the first postnatal week. *J*
752 *Neurophysiol* 124: 703-14

753 Jiang X, Lautermilch NJ, Watari H, Westenbroek RE, Scheuer T, Catterall WA. 2008. Modulation of CaV2.1
754 channels by Ca^{2+}/calmodulin-dependent protein kinase II bound to the C-terminal domain. *Proc*
755 *Natl Acad Sci U S A* 105: 341-6
756 Johnson BD, Scheuer T, Catterall WA. 1994. Voltage-dependent potentiation of L-type Ca2+ channels in
757 skeletal muscle cells requires anchored cAMP-dependent protein kinase. *Proceedings of the*
758 *National Academy of Sciences* 91: 11492-96
759 Kennedy MB. 1989. Regulation of neuronal function by calcium. *Trends Neurosci* 12: 417-20
760 Khorkova O, Golowasch J. 2007. Neuromodulators, not activity, control coordinated expression of ionic
761 currents. *J Neurosci* 27: 8709-18
762 Kourrich S, Calu DJ, Bonci A. 2015. Intrinsic plasticity: an emerging player in addiction. *Nature Reviews*
763 *Neuroscience* 16: 173-84
764 LeMasson G, Marder E, Abbott L. 1993. Activity-dependent regulation of conductances in model
765 neurons. *Science* 259: 1915-17
766 Levitan IB. 1988. Modulation of ion channels in neurons and other cells. *Annu Rev Neurosci* 11: 119-36
767 Li Y, Zaydman MA, Wu D, Shi J, Guan M, et al. 2011. KCNE1 enhances phosphatidylinositol 4,5-
768 bisphosphate (PIP2) sensitivity of IKs to modulate channel activity. *Proceedings of the National*
769 *Academy of Sciences* 108: 9095-100
770 Liu Z, Golowasch J, Marder E, Abbott LF. 1998. A Model Neuron with Activity-Dependent Conductances
771 Regulated by Multiple Calcium Sensors. *The Journal of Neuroscience* 18: 2309-20
772 MacLean JN, Zhang Y, Goeritz ML, Casey R, Oliva R, et al. 2005. Activity-independent coregulation of IA
773 and Ih in rhythmically active neurons. *J Neurophysiol* 94: 3601-17
774 Marom S. 2010. Neural timescales or lack thereof. *Prog Neurobiol* 90: 16-28
775 McCormick DA, Prince DA. 1987. Post-natal development of electrophysiological properties of rat
776 cerebral cortical pyramidal neurones. *J Physiol* 393: 743-62
777 Mizrahi A, Dickinson PS, Kloppenburg P, Fenelon V, Baro DJ, et al. 2001. Long-term maintenance of
778 channel distribution in a central pattern generator neuron by neuromodulatory inputs revealed
779 by decentralization in organ culture. *J Neurosci* 21: 7331-9
780 Moody WJ, Bosma MM. 2005. Ion channel development, spontaneous activity, and activity-dependent
781 development in nerve and muscle cells. *Physiol Rev* 85: 883-941
782 O'Leary T, Williams AH, Franci A, Marder E. 2014. Cell types, network homeostasis, and pathological
783 compensation from a biologically plausible ion channel expression model. *Neuron* 82: 809-21
784 Picken Bahrey HL, Moody WJ. 2003. Early development of voltage-gated ion currents and firing
785 properties in neurons of the mouse cerebral cortex. *J Neurophysiol* 89: 1761-73
786 Sametsky EA, Disterhoft JF, Ohno M. 2009. Autophosphorylation of alphaCaMKII downregulates
787 excitability of CA1 pyramidal neurons following synaptic stimulation. *Neurobiol Learn Mem* 92:
788 120-3
789 Santin JM, Schulz DJ. 2019. Membrane voltage is a direct feedback signal that influences correlated ion
790 channel expression in neurons. *Current Biology* 29: 1683-88. e2
791 Siegel M, Marder E, Abbott LF. 1994. Activity-dependent current distributions in model neurons. *Proc*
792 *Natl Acad Sci U S A* 91: 11308-12
793 Srikanth S, Narayanan R. 2015. Variability in State-Dependent Plasticity of Intrinsic Properties during
794 Cell-Autonomous Self-Regulation of Calcium Homeostasis in Hippocampal Model Neurons.
795 *eneuro* 2: ENEURO.0053-15.
796 Styr B, Slutsky I. 2018. Imbalance between firing homeostasis and synaptic plasticity drives early-phase
797 Alzheimer's disease. *Nature Neuroscience* 21: 463-73
798 Thoby-Brisson M, Simmers J. 2002. Long-term neuromodulatory regulation of a motor pattern-
799 generating network: maintenance of synaptic efficacy and oscillatory properties. *J Neurophysiol*
800 88: 2942-53

801 Tsitouras C. 2011. Runge–Kutta pairs of order 5 (4) satisfying only the first column simplifying
802 assumption. *Computers & Mathematics with Applications* 62: 770-75
803 Turrigiano G, Abbott LF, Marder E. 1994. Activity-dependent changes in the intrinsic properties of
804 cultured neurons. *Science* 264: 974-7
805 Turrigiano G, LeMasson G, Marder E. 1995. Selective regulation of current densities underlies
806 spontaneous changes in the activity of cultured neurons. *J Neurosci* 15: 3640-52
807 Viteri JA, Schulz DJ. 2023. Motor neurons within a network use cell-type specific feedback mechanisms
808 to constrain relationships among ion channel mRNAs. *Journal of Neurophysiology* 130: 569-84
809 Wang B, Brenner R. 2006. An S6 Mutation in BK Channels Reveals β1 Subunit Effects on Intrinsic and
810 Voltage-dependent Gating. *The Journal of General Physiology* 128: 731-44
811 Weiss S, Oz S, Benmocha A, Dascal N. 2013. Regulation of Cardiac L-Type Ca^{2+} Channel CaV1.2 Via the β-
812 Adrenergic-cAMP-Protein Kinase A Pathway. *Circulation Research* 113: 617-31
813 Wu LY, Song YJ, Zhang CL, Liu J. 2023. K(V) Channel-Interacting Proteins in the Neurological and
814 Cardiovascular Systems: An Updated Review. *Cells* 12
815 Zaccolo M, Benedetto D, G., Lissandron V, Mancuso L, Terrin A, Zamparo I. 2006. Restricted diffusion of
816 a freely diffusible second messenger: mechanisms underlying compartmentalized cAMP
817 signalling. *Biochemical Society Transactions* 34: 495-97

818

819

820

821 Box 1

Model Components

- *Neuron Model*
  - Hodgkin-Huxley representation of a single compartment neuron - voltage- and Ca- dependent currents plus leak
  - Basic $[Ca^{2+}]_i$ handling

- *Ca^{2+} Sensors*
  - Three different sensors that reflect $[Ca^{2+}]_i$ associated with slow wave of activity (*S*), spiking activity (*F*) and the average during a burst (*D*).
  - Targets are set for each sensor independently
  - The three different sensor values are compared to their target values and computed into a single score (α) that reflects the degree to which each is satisfied.

- *Homeostatic Mechanisms*
  - α is used to adjust the maximal conductances on a time scale τ_g and shifts in half-(in)activations voltages on a time scale of τ_{half}

822

823

Box 1, Supplement 1

$$(1)\quad C\frac{dV}{dt} = -\sum_{i=1}^{7} \bar{g}_i m_i^{q_i} h_i (V - E_i) - g_L(V - E_L) + I_{app}$$

$$(2)\quad \frac{dm_i}{dt} = \frac{m_{i,\infty}\left(V - V_{s_i^m}\right) - m_i}{\tau_{m_i}(V - V_{s_i^m})}$$

$$(3)\quad \frac{dh_i}{dt} = \frac{h_{i,\infty}\left(V - V_{s_i^h}\right) - h_i}{\tau_{h_i}(V - V_{s_i^h})}$$

$$(4)\quad \frac{d[Ca^{2+}]_i}{dt} = \frac{1}{20}(-.94\,(I_{CaT} + I_{CaS}) - [Ca^{2+}]_i + .05)$$

$$(5)\quad E_{Ca}([Ca^{2+}]_i) = 12.197 * log\left(\frac{[Ca^{2+}]_i}{3000.0}\right)$$

I_{CaT} and I_{CaS} are the $i = 2$ and $i = 3$ parts of the sum in Equation 1.

Table 1 – Activation Curve Exponents & Equilibrium Potentials

Current	Index (i)	q_i	E (mV)
I_{Na}	1	3	30
I_{CaT}	2	3	[set by Nernst Equation – Equation 5]
I_{CaS}	3	3	[set by Nernst Equation – Equation 5]
I_H	4	1	-20
I_{Kd}	5	4	-80
I_{KCa}	6	4	-80
I_A	7	3	-80

Table 2 – Normative values of Half-Activation and Half-Inactivation used to generate all starting parameter sets by randomized shifts. Final parameter sets are converted to the normative value minus the shift.

Current	Index (i)	$V_{\widehat{m}^0_{i,1/2}}$ (mV)	$V_{\widehat{h}^0_{i,1/2}}$ (mV)
I_{Na}	1	-25.5	-48.9
I_{CaT}	2	-27.1	-32.1
I_{CaS}	3	-33	-60
I_H	4	-70	
I_{Kd}	5	-12.3	
I_{KCa}	6	-28.3	
I_A	7	-27.2	-56.9

Table 3 – Activation Curves and Associated Time Constants

Current	$m_{i,\infty}$ (mV)	τ_{m_i} (ms)
I_{Na}	$\frac{1}{1+\exp\left(\frac{V-\left(V_{\hat{m}^0_{1,1/2}}+V_{s_1^m}\right)}{-5.29}\right)}$	$1.32-\frac{1.26}{1+\exp\left(\frac{\left(V-V_{s_1^m}\right)+120}{-25}\right)}$
I_{CaT}	$\frac{1}{1+\exp\left(\frac{V-\left(V_{\hat{m}^0_{2,1/2}}+V_{s_2^m}\right)}{-7.2}\right)}$	$21.7-\frac{21.3}{1+\exp\left(\frac{\left(V-V_{s_2^m}\right)+68.1}{-20.5}\right)}$
I_{CaS}	$\frac{1}{1+\exp\left(\frac{V-\left(V_{\hat{m}^0_{3,1/2}}+V_{s_3^m}\right)}{-8.1}\right)}$	$1.4+\frac{7}{\exp\left(\frac{\left(V-V_{s_3^m}\right)+27}{10}\right)+\exp\left(\frac{\left(V-V_{s_3^m}\right)+70}{-13}\right)}$
I_H	$\frac{1}{1+\exp\left(\frac{V-\left(V_{\hat{m}^0_{4,1/2}}+V_{s_4^m}\right)}{6}\right)}$	$272-\frac{-1499}{1+\exp\left(\frac{\left(V-V_{s_4^m}\right)+42.2}{-8.73}\right)}$
I_{Kd}	$\frac{1}{1+\exp\left(\frac{V-\left(V_{\hat{m}^0_{5,1/2}}+V_{s_5^m}\right)}{-11.8}\right)}$	$7.2-\frac{6.4}{1+\exp\left(\frac{\left(V-V_{s_5^m}\right)+28.3}{-19.2}\right)}$
I_{KCa}	$\frac{1}{1+\exp\left(\frac{V-\left(V_{\hat{m}^0_{6,1/2}}+V_{s_6^m}\right)}{-12.6}\right)}\frac{[Ca^{2+}]_i}{[Ca^{2+}]_i+3}$	$90.3-\frac{75.1}{1+\exp\left(\frac{\left(V-V_{s_6^m}\right)+46}{-22.7}\right)}$
I_A	$\frac{1}{1+\exp\left(\frac{V-\left(V_{\hat{m}^0_{7,1/2}}+V_{s_7^m}\right)}{-8.7}\right)}$	$11.6-\frac{10.4}{1+\exp\left(\frac{\left(V-V_{s_7^m}\right)+32.9}{-15.2}\right)}$

Table 4 – Inactivation Curves and Associated Time Constants

Current	$h_{i,\infty}$ (mV)	τ_{h_i} (ms)
I_{Na}	$\frac{1}{1+\exp\left(\frac{V-\left(V_{\hat{h}^0_{1,1/2}}+V_{s_1^h}\right)}{5.18}\right)}$	$\left(1.5-\frac{-1}{1+\exp\left(\frac{\left(V-V_{s_1^h}\right)+34.9}{3.6}\right)}\right)\left(\frac{.67}{1+\exp\left(\frac{\left(V-V_{s_1^h}\right)+62.9}{-10}\right)}\right)$
I_{CaT}	$\frac{1}{1+\exp\left(\frac{V-\left(V_{\hat{h}^0_{2,1/2}}+V_{s_2^h}\right)}{5.5}\right)}$	$105-\frac{89.8}{1+\exp\left(\frac{\left(V-V_{s_2^h}\right)+55.0}{-16.9}\right)}$
I_{CaS}	$\frac{1}{1+\exp\left(\frac{V-\left(V_{\hat{h}^0_{3,1/2}}+V_{s_3^h}\right)}{6.2}\right)}$	$60+\frac{150}{\exp\left(\frac{\left(V-V_{s_3^h}\right)+55}{9}\right)+\exp\left(\frac{\left(V-V_{s_3^h}\right)+65}{-16}\right)}$
I_H	1	1
I_{Kd}	1	1
I_{KCa}	1	1
I_A	$\frac{1}{1+\exp\left(\frac{V-\left(V_{\hat{h}^0_{7,1/2}}+V_{s_7^h}\right)}{4.9}\right)}$	$38.6-\frac{29.2}{1+\exp\left(\frac{\left(V-V_{s_7^h}\right)+38.9}{-26.5}\right)}$

Box 1, Supplement 2

$$(6)\quad \frac{dM_X}{dt} = \frac{\bar{M}_X\,(I_{CaT} + I_{CaS}) - M_X}{\tau_{M_X}}\ ; X = F, S, D$$

$$(7)\quad \frac{dH_X}{dt} = \frac{\bar{H}_X\,(I_{CaT} + I_{CaS}) - H_X}{\tau_{H_X}}\ ; X = F, S, D$$

$$(8)\quad F = G_F M_F^2 H_F \quad S = G_S M_S^2 H_S \quad D = G_D M_D^2$$

$$(9)\quad \frac{dE_F}{dt} = \frac{(F - \bar{F}) - E_F}{\tau_S}$$

$$(10)\quad \frac{dE_S}{dt} = \frac{(S - \bar{S}) - E_S}{\tau_S}$$

$$(11)\quad \frac{dE_D}{dt} = \frac{(D - \bar{D}) - E_D}{\tau_S}$$

$$(12)\quad S_f = e^{-((E_F/\Delta_F)^8 + (E_D/\Delta_D)^8 + (E_S/\Delta_S)^8)^{1/8}}$$

$$(13)\quad \tau_\alpha \frac{d\alpha}{dt} = \alpha_\infty(S_f) - \alpha$$

$$(14)\quad \alpha_\infty(S_f) = \frac{1}{1 + e^{\frac{-(S_f + \rho)}{\Delta_\alpha}}}$$

G_F, G_S and G_D are set to 53, 3, and 1, respectively. Also, $\Delta_F = .1$, $\Delta_S = .008$, and $\Delta_D = .015$. During simulations involving increased extracellular potassium concentration Δ_D is increased to $.035$

Table 1 – M_X Parameters and Time Constants

$\bar{M}_X$ is a sigmoid function with centering parameter Z:

$$\bar{M}_X = \frac{1}{1 + \exp\left(Z + (I_{CaT} + I_{CaS})\right)}$$

	Z	τ_{M_X}
F	14.8	0.5
S	7.2	50

D	3	500

Table 2 – H_X Parameters and Time Constants

$\bar{H}_X$ is a sigmoid function with centering parameter Z:

$$\bar{H}_X = \frac{1}{1 + \exp\left(-Z - (I_{CaT} + I_{CaS})\right)}$$

	Z	τ_{H_X}
F	9.8	1.5
S	2.8	60
D	-	-

Box 1, Supplement 3

$$(15)\quad \frac{\tau_g}{\alpha}\frac{d\bar{g}_i}{dt} = [A_i(\bar{F}-F) + B_i(\bar{S}-S) + C_i(\bar{D}-D)]\bar{g}_i - \gamma\bar{g}_i^3$$

$$(16)\quad \frac{\tau_{half}}{\alpha}\frac{dV_{s_i^m}}{dt} = [\hat{A}_i(\bar{F}-F) + \hat{B}_i(\bar{S}-S) + \hat{C}_i(\bar{D}-D)] \quad - \hat{\gamma}\left(V_{s_i^m}\right)^3$$

$$(17)\quad \frac{\tau_{half}}{\alpha}\frac{dV_{s_i^h}}{dt} = [\hat{\hat{A}}_i(\bar{F}-F) + \hat{\hat{B}}_i(\bar{S}-S) + \hat{\hat{C}}_i(\bar{D}-D)] \quad - \hat{\gamma}\left(V_{s_i^h}\right)^3$$

Table 1: Parameters describing Homeostatic Modulation of Intrinsic Current Properties (Li Matrix)

Current	Index (i)	A_i	B_i	C_i	$\hat{A}_i$	$\hat{B}_i$	$\hat{C}_i$	$\hat{\hat{A}}_i$	$\hat{\hat{B}}_i$	$\hat{\hat{C}}_i$
I_{Na}	1	+1	0	0	-1	0	0	+1	0	0
I_{CaT}	2	0	+1	0	0	-1	0	0	+1	0
I_{CaS}	3	0	+1	0	0	-1	0	0	+1	0
I_H	4	+1	-1	0	-1	+1	0	+1	-1	0
I_{Kd}	5	0	-1	-1	0	+1	+1	0	-1	-1
I_{KCa}	6	0	-1	-1	0	+1	+1	0	-1	-1
I_A	7	0	+1	+1	0	-1	-1	0	+1	+1

In this paper, the values $\hat{A}_i$, $\hat{B}_i$, and $\hat{C}_i$ are the negative of A_i, B_i, and C_i, respectively. The values $\hat{\hat{A}}_i$, $\hat{\hat{B}}_i$, and $\hat{\hat{C}}_i$ are equal to A_i, B_i, and C_i, respectively. The manner at which we arrive at these values are outlined in Methods. As outlined in Discussion, these coefficients do not need to take these values.

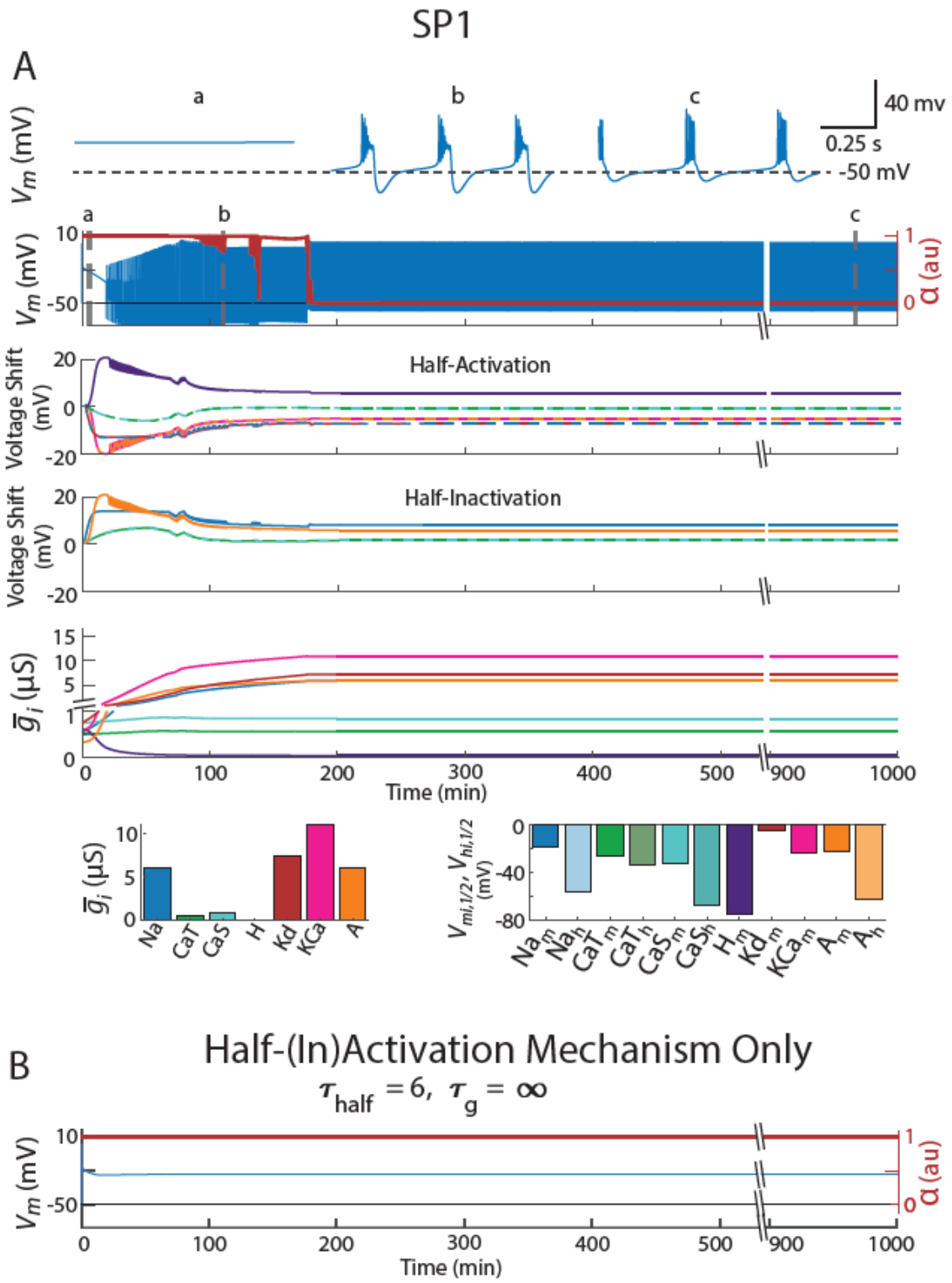
SP1
A
a
b
c
40 mv
0.25 s
-50 mV
V_m (mV)
10
-50
1
0
α (au)
Half-Activation
Voltage Shift (mV)
20
0
-20
Half-Inactivation
$\bar{g}_i$ (μS)
15
10
5
1
0
100
200
300
400
500
900
1000
Time (min)
Na
CaT
CaS
H
Kd
KCa
A
$V_{mi,1/2}, V_{hi,1/2}$ (mV)
-40
-80
Na_m
Na_h
CaT_m
CaT_h
CaS_m
CaS_h
H_m
Kd_m
KCa_m
A_m
A_h
B
Half-(In)Activation Mechanism Only
$\tau_{half} = 6, \ \tau_g = \infty$

Figure 1 – Activity-Dependent Regulation Mechanism ($\tau_{half} = 6$ s and $\tau_g = 600$ s) was used to assemble a burster that meets the Ca^{2+} targets from 'random' starting parameters (i.e. SP). Both this set of starting parameters and its resultant model are called SP1. A – Row 1: blow-ups of specific points a, b, and c in the voltage trace in Row 2. Row 2: The neuron's electrical activity as its channel density and (in)activations curves were being adjusted. α is a measure of how close the model is to satisfying Ca^{2+} targets (see Methods). It took values between 0 and 1, with 0 meaning the targets were satisfied. Row 3: Plots the adjustments made to the half-activations as the model attempted to satisfy the calcium targets. They are color-coded to match the intrinsic currents shown in the left plot of Row 5. Row 4: Same as Row 3, except for (in)activation curves. Note that not all currents in this model have inactivation curves. Row 5: Same as Row 3, except for maximal conductances (i.e. channel density). Row 6: The final levels of maximal conductances are shown in the left plot. The final half-(in)activations are plotted on the right. The final half-activation of an intrinsic current, $V_{m_{i,1/2}}$, was the sum of the initially posited level of the that current's half-activation $V_{\hat{m}^0_{i,1/2}}$ and the shifts the model made to the activation curve, $V_{s_i^m}$ (shown in Row 3). The final half-inactivation of an intrinsic current, $V_{h_{i,1/2}}$, was the sum of the initially posited level of the that current's half-inactivation $V_{\hat{h}^0_{i,1/2}}$ and the shifts the model made to the inactivation curve, $V_{s_i^h}$ (shown in Row 4). [The process is illustrated in Figure 1 (supplement 1) for a different set of starting parameters (i.e. initial half-(in)activation shifts and maximal conductance levels).] B – This displays the neuron's electrical activity if the model was restricted to varying only half-(in)activations ($\tau_{half} = 6$ s), with maximal conductances fixed ($\tau_g = \infty$ s). The same starting parameters as in Panel A were used for this simulation.

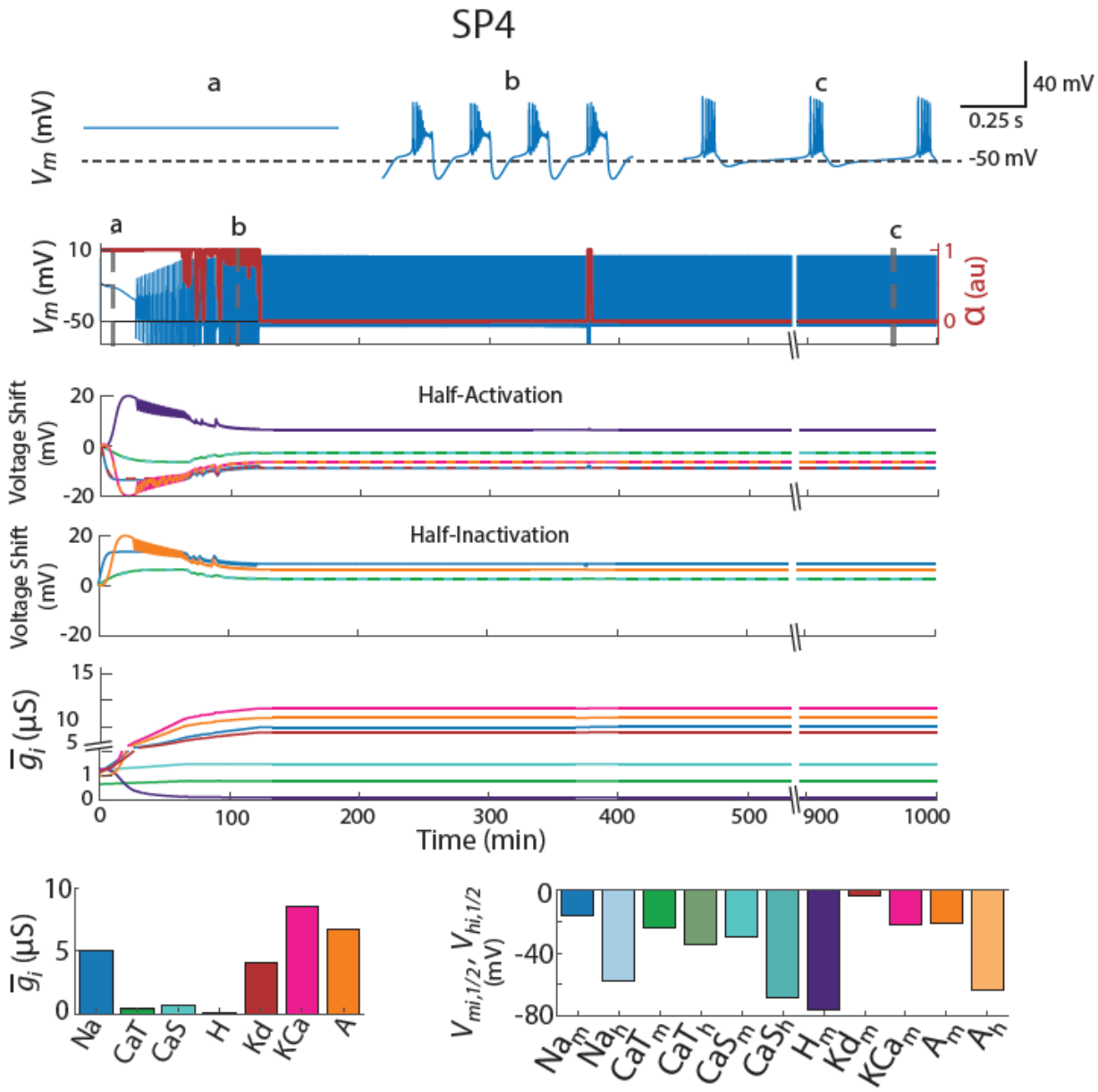

Figure 1 (Supplement) – This model attempts to satisfy the same Ca^{2+} targets as in Figure 1, Panel A, but was started from a different set of 'random' initial parameters. The rows correspond to those in Figure 1, Panel A. Note that the maximal conductances of the two potassium currents, I_{Kd} and I_A, differ from SP1.

920

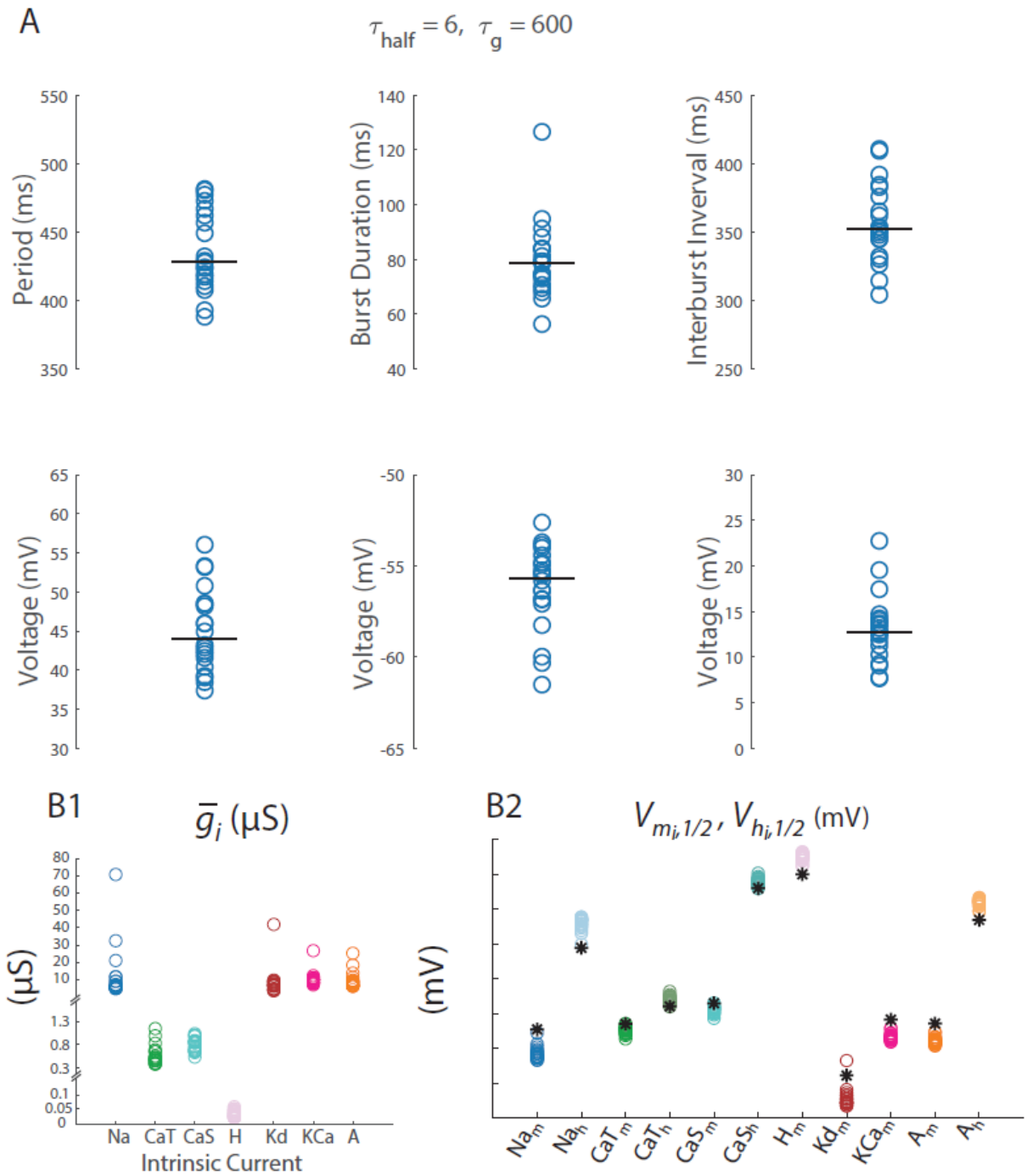

Figure 2 – All 20 SP's were analyzed including those illustrated in Figure 1. A) The top left panel displays the periods for all SP's. Burst Duration, Interburst Interval, Spike Hight, Maximum Hyperpolarization, and Slow Wave Amplitude measurements for these

925 SP's are provided in subsequent plots. B) B1 shows maximal conductances, and B2
926 displays half-(in)activation voltages for each of the 20 SP's. An asterisk on the right
927 indicates the initially specified level of half-(in)activation from which random deviations
928 were made.

929

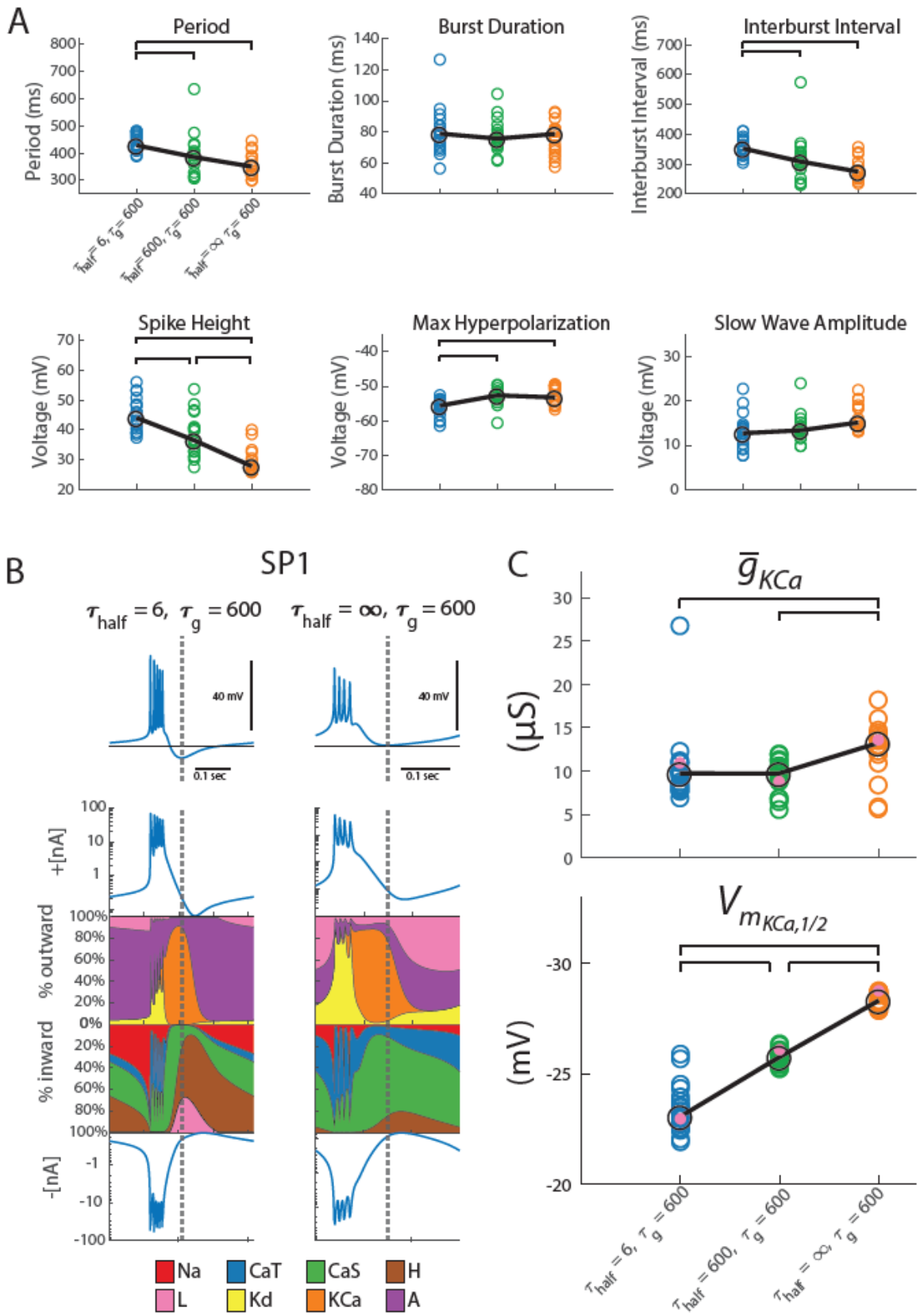
A
Period
Period (ms)
Burst Duration
Burst Duration (ms)
Interburst Interval
Interburst Interval (ms)
Spike Height
Voltage (mV)
Max Hyperpolarization
Voltage (mV)
Slow Wave Amplitude
Voltage (mV)
B
SP1
40 mV
0.1 sec
+[nA]
% outward
% inward
-[nA]
Na
CaT
CaS
H
L
Kd
KCa
A
C
(μS)
(mV)

930

Figure 3 - The speed at which the model changed half-(in)activations in response to deviations from Ca^{2+} target impacted the type of bursters the model assembled. In all simulation for this figure, $\tau_g = 600$. A) These plots extend the measurements from Figure 2 to the same 20 SP's, now with half-(in)activations regulated at a different speed. In blue, $\tau_{half} = 6$ s; recapitulating results in Figure 2. In green and orange, the SP's were reassessed with slower half-(in)activation adjustments, $\tau_{half} = 600$ s, and $\tau_{half} = \infty$ s (i.e. halted), respectively. Brackets indicate significant differences in medians ($p < .05$). These pairwise differences were assessed using a Kruskal-Wallis test (to assess whether any differences in medians existed between all groups) and post-hoc Dunn tests with Bonferroni corrections to assess which pairs of groups differed significantly in their medians. B) The model was used to stabilize SP1 to the same Ca^{2+} target but using different timescales of half-(in)activation alterations. $\tau_{half} = 6$ s is shown on the left and $\tau_{half} = \infty$ s (representing the slowest possible response) on the right. Rows 1-4 below each voltage trace show: the total outward current, percentage contribution of each outward intrinsic current to the total outward current, percentage contribution of each inward intrinsic current to the total inward current, and the total inward current. A dashed vertical line across all rows marks the point of maximum hyperpolarization in each activity pattern to guide focused comparison. C) When the model stabilized around a burster, the speed at which the model changed half-(in)activations impacted maximal conductance and half-activation location of the calcium-activated potassium current. Shown here in blue, green, and orange are $\tau_{half} = 6$ s, $\tau_{half} = 600$ s, and $\tau_{half} = \infty$ s (i.e. halted), respectively. SP1 – SP20 are in the colored circles. Trends are illustrated with a black line, with large circles marking

954 median positions. The mauve dot highlights the levels to which maximal conductance
955 and half-(in)activation of SP1 evolved. The asterisks mark the original position of the
956 KCa half-activation ($V_{\widehat{m}^0_{6,1/2}}$). A Kruskal-Wallis test followed by post-hoc Dunn tests
957 (with Bonferroni corrections) were conducted to assess significant ($p < .05$) pairwise
958 differences in medians (brackets).

959

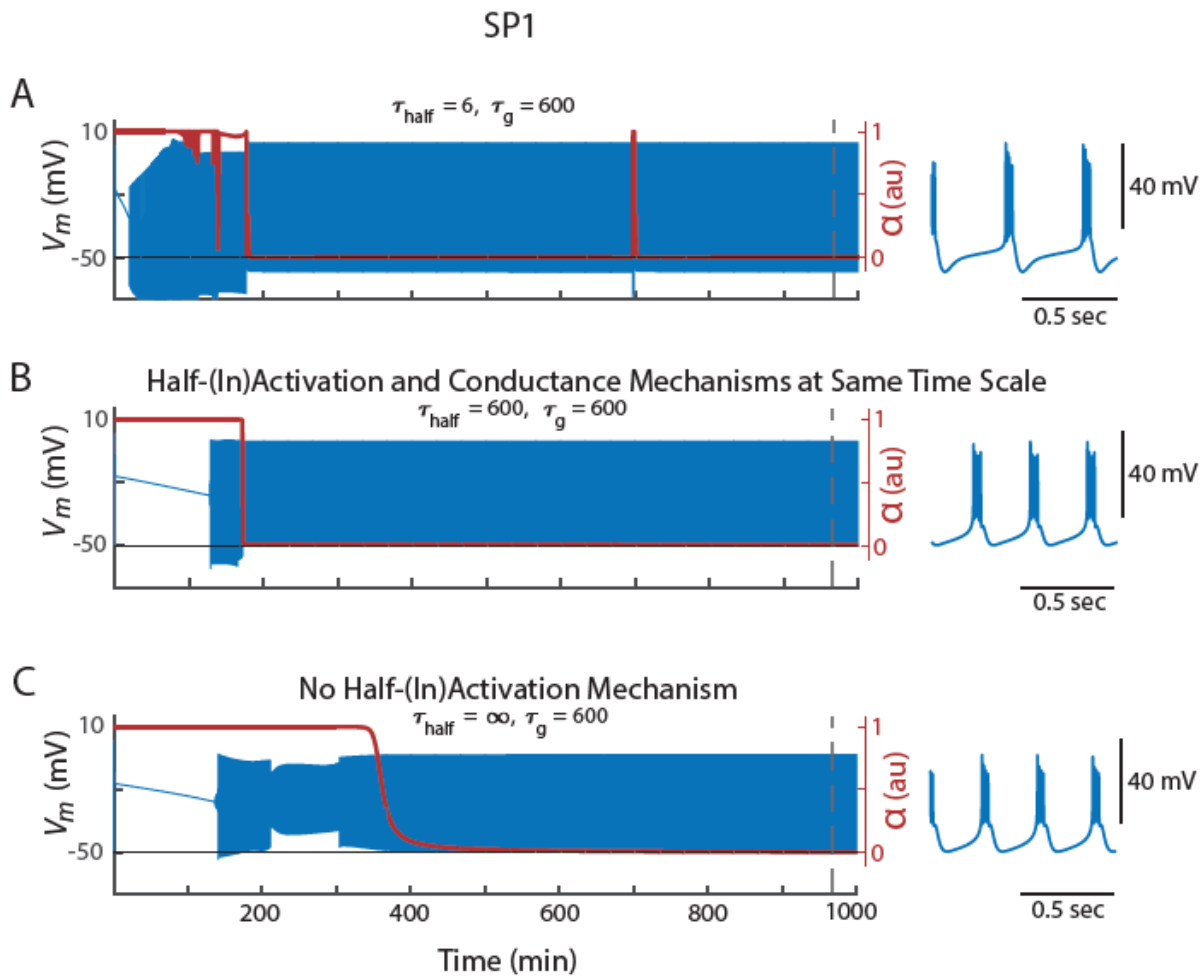

Figure 4 – Changes to the timescale of half-(in)activation alterations steers the model through different trajectories in intrinsic parameter space. Each row shows the behavior of Starting Parameter 1 (SP1) as the model adjusts toward a configuration that satisfies the calcium activity target, using different timescales for half-(in)activation regulation. A – $\tau_{half} = 6$ s, B – $\tau_{half} = 600$ s, C –$\tau_{half} = \infty$ s (i.e. half-(in)activations do not change). In all panels, the speed at which the model changed channel density is fixed in all rows: $\tau_g = 600$ s. Superimposed on these traces is the α parameter, which indicates whether the activity patterns were meeting the Ca^{2+} targets. Blow-ups of the activity pattern when the calcium sensors were satisfied are displayed to the right.

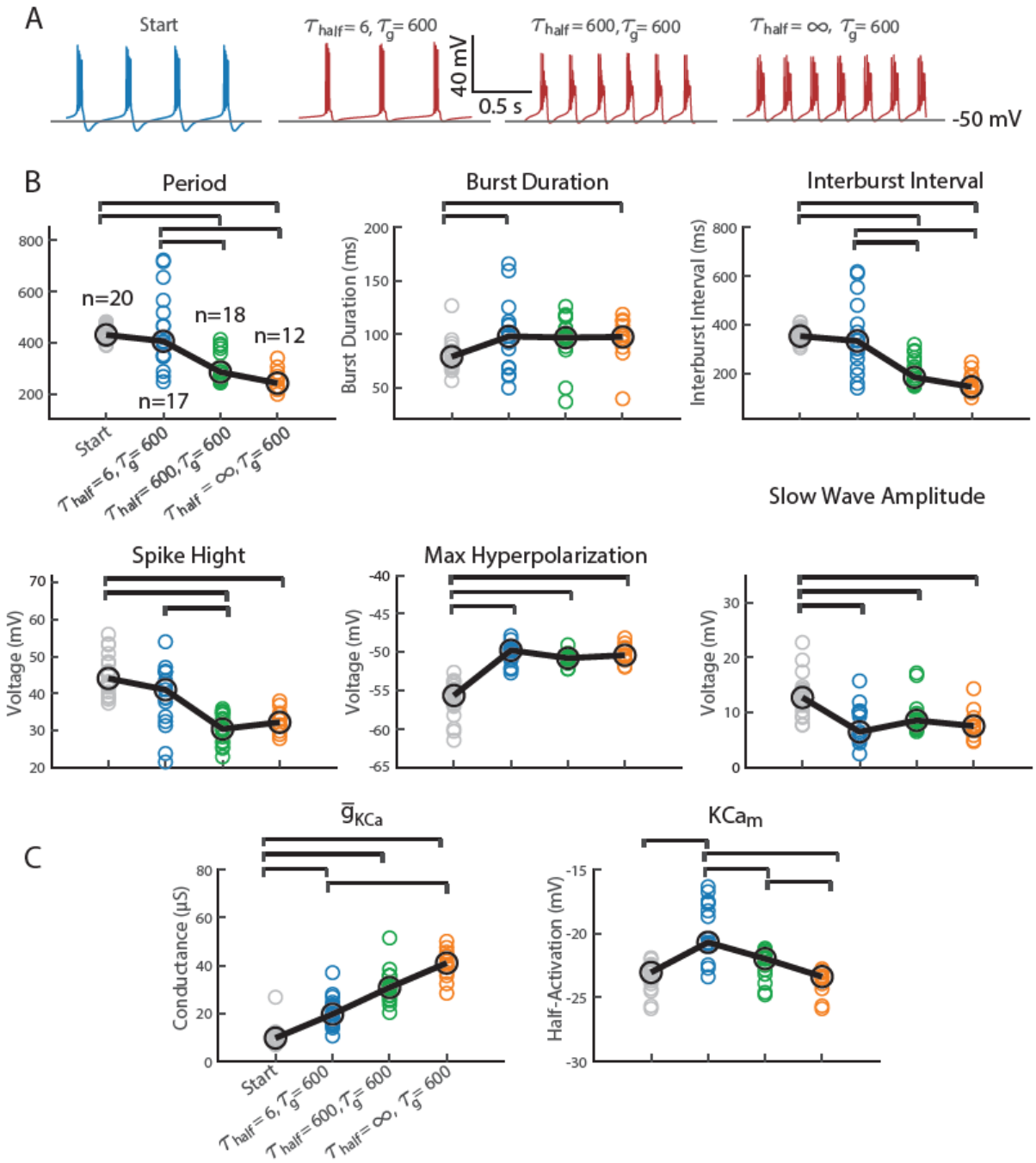

Figure 5 – The speed at which the model changed half-(in)activations in response to deviations from Ca^{2+} targets impacted the type of bursters the model assembled following perturbation. A) Voltage traces from SP1 before (blue) and 265 minutes after (red) a simulated increase in extracellular potassium concentration. Each panel shows

recovery under a different timescale for half-(in)activation regulation: fast ($\tau_{half} = 6$ s), intermediate ($\tau_{half} = 600$ s), and infinitely slow (i.e. off, $\tau_{half} = \infty$ s). In all condition, alteration of maximal conductances was held fixed ($\tau_g = 600$ s). B) Summary of activity features for all SP1–SP20 models that recovered to a stable burst pattern. The number of models that successfully recovered varied with the homeostatic mechanism: fast (n = 17), intermediate (n = 18), and no half-(in)activation modulation (n = 20). Gray points indicate pre-perturbation measurements of SP1-20 (from Figure 3A). Significant pairwise differences in median values were assessed using a Kruskal–Wallis test followed by post hoc Dunn tests with Bonferroni correction. Significant comparisons ($p < 0.05$) are marked with horizontal brackets. C) The speed of half-(in)activation regulation influenced both the maximal conductance and half-activation voltage of KCa. Data are grouped by as they are in B). Statistical comparisons were performed as in B).

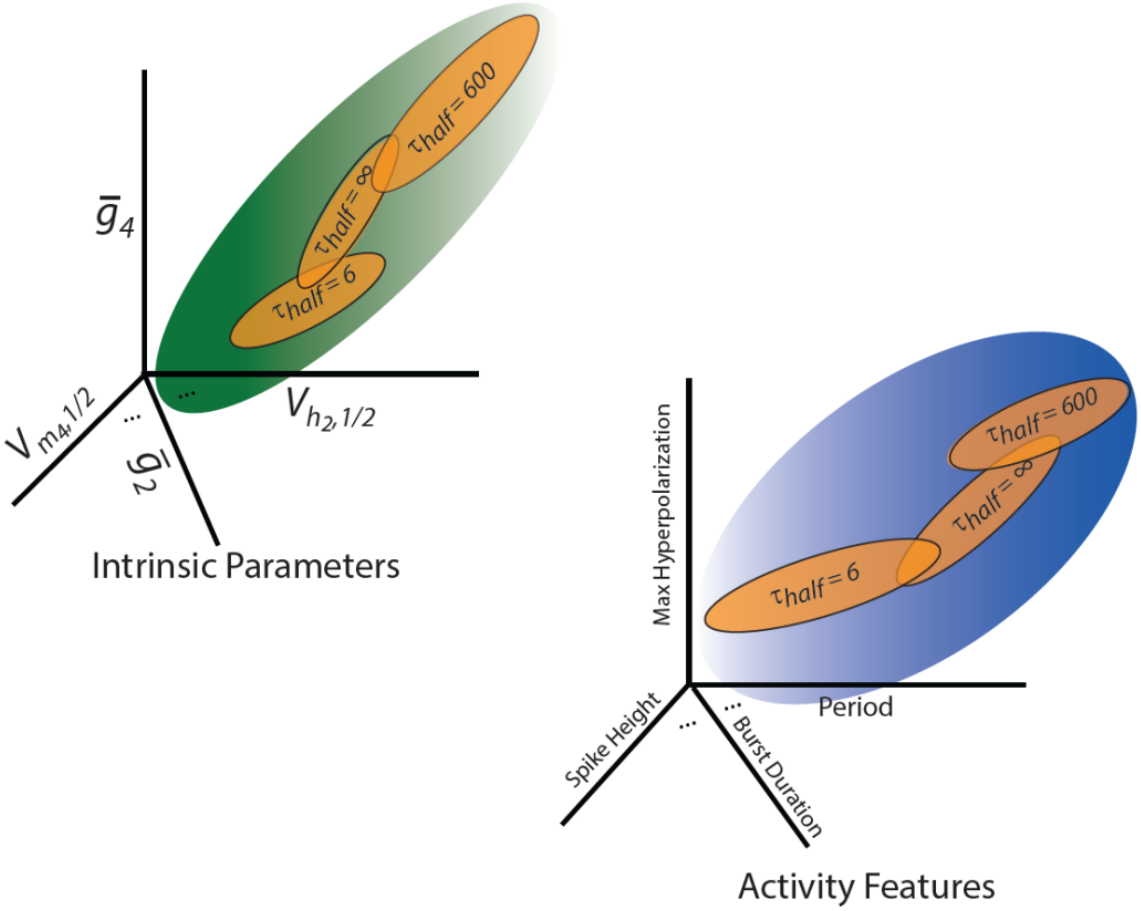

Figure 6 – The impact of adjusting the timescale of ion channel (in)activation curve alterations can be illustrated conceptually using the space of activity characteristics (right) and underlying intrinsic parameters (left). The regions in green and blue are the activity patterns that are consistent with the Ca^{2+} targets in the space of activity characteristics and underlying intrinsic parameters, respectively. As the rate of ion channel half-(in)activation adjustments in response to deviations from Ca^{2+} targets is changed, the regions targeted by the model also shift (shown in orange). Regardless of

996 the timescale, all targeted regions reside within a larger region encompassing all activity

997 profile measurements and intrinsic parameters consistent with the Ca^{2+} targets.

998

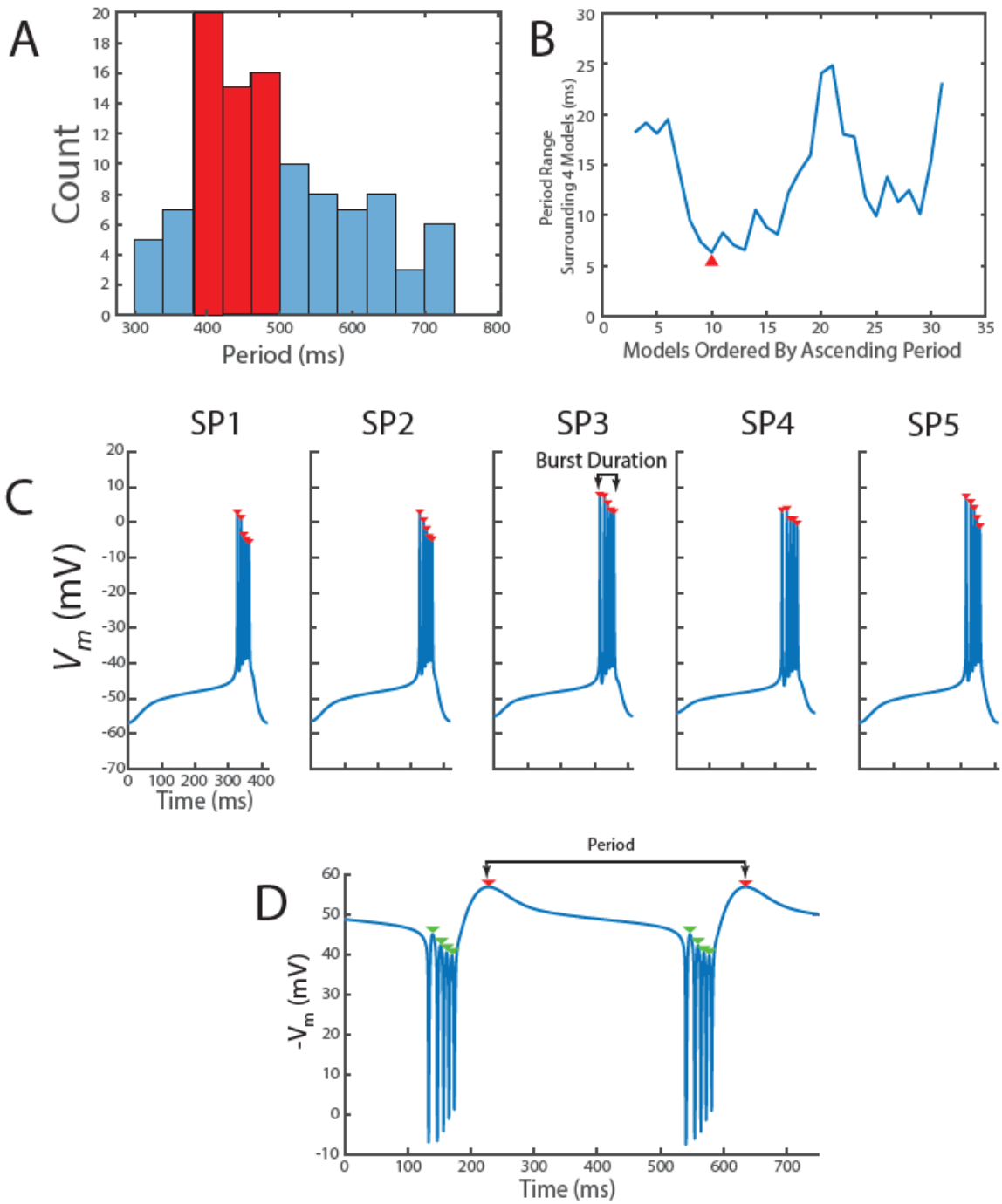

Figure 7 – We constructed the Group of 20 Bursters by selecting a putative representative of the entire population and then identifying bursters with similar

activity patterns. A) - 111 bursters were narrowed to 80 bursters by excluding certain characteristics (see Methods). These models had a period distribution shown in A. Highlighted in red are the models chosen for further selection. B) This plot illustrates how closely the periods of the models chosen in A align with their two neighbors after they were ordered from smallest to largest. The first model, SP1, was chosen as the neuron with neighbors that also have close periods (red arrow). C) - To assemble the Group of 20, we symmetrically expanded the inter-instance period range around SP1's period by 20%. SP2-SP5's wave forms are shown. Depolarizing excursions (spikes) were detected using MATLAB's findpeaks function with a prominence threshold of 2 (red arrows). D) – Troughs were identified using the findpeaks function on the negative waveform of a cycle period, applying the same prominence threshold. The detected troughs are indicated by red arrows. The example displayed here represents the inverted voltage trace of the burster assembled by the model from SP1. The period was measured as the time difference between successive points of maximum hyperpolarization.